

Characterizing sources of high surface ozone events in the southwestern U.S. with intensive field measurements and two global models

Li Zhang^{1,2}, Meiyun Lin^{1,2*}, Andrew O. Langford³, Larry W. Horowitz², Christoph J. Senff^{3,4}, Elizabeth Klovenski⁵, Yuxuan Wang⁵, Raul J. Alvarez II³, Irina Petropavlovskikh^{4,6}, Patrick Cullis^{4,6}, Chance W. Sterling^{4,6,7}, Jeff Peischl^{3,4}, Thomas B. Ryerson³, Steven S. Brown^{3,8}, Zachary C.J. Decker^{3,4,8}, Guillaume Kirgis^{3,4}, Stephen Conley⁹

¹Program in Atmospheric and Oceanic Sciences, Princeton University, Princeton, NJ, USA;

²NOAA Geophysical Fluid Dynamics Laboratory, Princeton, NJ, USA;

³NOAA Chemical Science Laboratory, Boulder, CO, USA;

⁴Cooperative Institute for Research in Environmental Sciences, University of Colorado, Boulder, CO, USA;

⁵Department of Earth and Atmospheric Sciences, University of Houston, Houston, TX, USA;

⁶NOAA Global Monitoring Laboratory, Boulder, CO, USA

⁷C&D Technologies Inc., Philadelphia, PA, USA;

⁸Department of Chemistry, University of Colorado, Boulder, CO, USA;

⁹Scientific Aviation Inc., Boulder, CO, USA

Corresponding author: Meiyun Lin (meiyun.lin@noaa.gov)

Abstract

The detection and attribution of high background ozone (O_3) events in the southwestern U.S. is challenging but relevant to the effective implementation of the lowered National Ambient Air Quality Standard (NAAQS; 70 ppbv). Here we leverage intensive field measurements from the Fires, Asian, and Stratospheric Transport–Las Vegas Ozone Study (*FAST-LVOS*) in May–June 2017, alongside high-resolution simulations with two global models (GFDL-AM4 and GEOS-Chem), to pinpoint the sources of O_3 during high- O_3 events. We show stratospheric influence on four out of the ten events with daily maximum 8-hour average (MDA8) surface O_3 above 65 ppbv in the greater Las Vegas region. While O_3 produced from regional anthropogenic emissions dominates pollution events in the Las Vegas Valley,

stratospheric intrusions can mix with regional pollution to push surface O₃ above 70 ppbv. GFDL-AM4 captures the key characteristics of deep stratospheric intrusions consistent with ozonesondes, lidar profiles, and co-located measurements of O₃, CO, and water vapor at Angel Peak, whereas GEOS-Chem has difficulty simulating the observed features and underestimates observed O₃ by ~20 ppbv at the surface. On days when observed MDA8 O₃ exceeds 65 ppbv and AM4 stratospheric ozone tracer shows 20-40 ppbv enhancements, GEOS-Chem simulates ~15 ppbv lower U.S. background O₃ than GFDL-AM4. The two models also differ substantially during a wildfire event, with GEOS-Chem estimating ~15 ppbv greater O₃, in better agreement with lidar observations. At the surface, the two models bracket the observed MDA8 O₃ values during the wildfire event. Both models capture the large-scale transport of Asian pollution, but neither resolves some fine-scale pollution plumes, as evidenced by aerosol backscatter, aircraft, and satellite measurements. U.S. background O₃ estimates from the two models differ by 5 ppbv on average (greater in GFDL-AM4) and up to 15 ppbv episodically. Our multi-model approach tied closely to observational analysis yields process insights, suggesting that elevated background O₃ may pose challenges to achieving a potentially lower NAAQS level (e.g., 65 ppbv) in the southwestern U.S.

Keywords: background ozone, stratospheric intrusions, wildfires, Asian pollution

1 Introduction

Surface ozone (O₃) typically peaks over the high-elevation southwestern U.S. (SWUS) in late spring, in contrast to the summer maximum produced from regional anthropogenic emissions in the low-elevation eastern U.S. (EUS). The springtime O₃ peak in the SWUS partly reflects the substantial influence of background O₃ from natural sources (e.g., stratospheric intrusions) and intercontinental pollution (Zhang et al., 2008; Fiore et al., 2014; Jaffe et al., 2018). These “non-controllable” O₃ sources can episodically push surface daily maximum 8-hour average (MDA8) O₃ to exceed the NAAQS (Lin et al., 2012a; Lin et al., 2012b; Langford et al., 2017). Identifying and quantifying the sources of springtime high-O₃ events in the SWUS has been extremely challenging owing to limited measurements, complex topography, and various O₃ sources (Langford et al., 2015). As the O₃ NAAQS becomes more stringent (lowered from 75 ppbv to 70 ppbv since 2015), quantitative understanding of background O₃ sources is of great importance for screening exceptional events, i.e., “unusual or naturally occurring events that can affect air quality but are not reasonably controllable using techniques that tribal, state or local air agencies may implement” (U.S. Environmental Protection Agency, 2016). Here we leverage intensive measurements from the 2017

Fires, Asian, and Stratospheric Transport-Las Vegas Ozone Study (*FAST-LVOS*; Langford et al., manuscript in preparation), alongside high-resolution simulations with two global atmospheric chemistry models (GFDL-AM4 and GEOS-Chem), to characterize the sources of high- O_3 events in the region. Through a process-oriented analysis, we aim to understand the similarities and disparities between these two widely-used global models in simulating O_3 in the SWUS.

Mounting evidence shows that a variety of sources contribute to the high surface O_3 found in the SWUS during spring. For example, observational and modelling studies show that deep stratospheric intrusions can episodically increase springtime MDA8 O_3 levels at high-elevation SWUS sites by 20–40 ppbv (Langford et al., 2009; Lin et al., 2012a). Large-scale transport of Asian pollution across the North Pacific also peaks in spring due to active mid-latitude cyclones and strong westerly winds, contributing to high- O_3 events and raising mean background O_3 levels over the SWUS (Jacob et al., 1999; Lin et al., 2012b; Lin et al., 2015b; Langford et al., 2017; Lin et al., 2017). Moreover, frequent wildfires complicate the study of O_3 in the SWUS (Jaffé et al., 2013; Baylon et al., 2016; Lin et al., 2017; Jaffé et al., 2018). In the late spring and early summer, increased photochemical activity from U.S. domestic anthropogenic emissions can prevent the unambiguous attribution of observed high- O_3 events in this region to background influence.

Quantifying the contributions of different O_3 sources relies heavily on numerical models. Previous studies, however, have shown large model discrepancies in the estimates of North American background O_3 (NAB), defined as O_3 that would exist in the absence of North American anthropogenic emissions. Zhang et al. (2011) applied GEOS-Chem to quantify NAB O_3 during March–August of 2006–2008 and estimated a mean of 40 ± 7 ppbv at SWUS high-elevation sites, while Lin et al. (2012a) estimated 50 ± 11 ppbv for the late spring to early summer of 2010 with GFDL-AM3. Emery et al. (2012) estimated mean NAB O_3 to be 20–45 ppbv with GEOS-Chem and 25–50 ppbv with a regional model driven by GEOS-Chem boundary conditions, during spring-summer. Large inter-model differences exist not only in seasonal means but also in day-to-day variability (e.g., Fiore et al., 2014; Dolwick et al., 2015; Jaffé et al., 2018). An event-oriented multi-model comparison, tied closely to intensive field measurements, is needed to provide process insights into this model discrepancy.

Deploying targeted measurements and conducting robust model source attribution are crucial to characterize and quantify the sources of elevated springtime O_3 in the SWUS (Langford et al., 2009;

Langford et al., 2012; Lin et al., 2012a; Lin et al., 2012b). This is particularly true for inland areas of the SWUS, such as greater Las Vegas, where air quality monitoring sites are sparse, making it difficult to assess the robustness of model source attribution (Langford et al., 2015; Langford et al., 2017). Using field measurements from the Las Vegas Ozone Study (LVOS) in May–June 2013 and model simulations, Langford et al. (2017) provided an unprecedented view of the influences of stratosphere-to-troposphere transport (STT) and Asian pollution on the exceedances of surface O₃ in Clark County, Nevada. This study suggests that O₃ descending from the stratosphere and sometimes mingled with Asian pollution can be entrained into the convective boundary layer and episodically brought down to the ground in the Las Vegas area in spring, adding 20–40 ppbv to surface O₃ and pushing MDA8 O₃ above the NAAQS. However, uncertainties remain in previous analyses due to the use of relatively coarse-resolution simulations and limited measurements to connect surface O₃ exceedances at high-elevation baseline sites and low-elevation regulatory sites. High-resolution simulations and more extensive observations are thus needed to further advance our understanding of springtime peak O₃ episodes in the region.

In May–June 2017, the NOAA Earth System Research Laboratory Chemical Sciences Division (NOAA/ESRL CSD) carried out the *FAST*-LVOS follow up study in Clark County, NV. During this campaign, a broad suite of near-continuous observations was collected by in situ chemistry sensors deployed at a mountain-top site and by state-of-the-art ozone and Doppler lidars located in the Las Vegas Valley. These daily measurements were supplemented by ozonesondes and scientific aircraft flights during four 2- to 4-day-long intensive operating periods (IOPs) triggered by the appearance of upper-level troughs above the U.S. West Coast. These extensive measurements, together with high-resolution simulations from two global models (GFDL-AM4 and GEOS-Chem), provide us with a rare opportunity to pinpoint the sources of elevated springtime O₃ in the SWUS. We briefly describe the *FAST*-LVOS field campaign and model configurations in Sect. 2. Following an overall model evaluation (Sect. 3), we present process-oriented analyses of the high-O₃ events from deep stratospheric intrusions, wildfires, regional anthropogenic pollution, and the long-range transport of Asian pollution (Sect. 4). Sect. 5 summarizes differences between the simulated total and background O₃ determined by the two models during *FAST*-LVOS. Finally, in Sect. 6, the implications of the study are discussed.

2 Measurements and Models

2.1 *FAST*-LVOS measurement campaign

[Figure 1 about here]

The *FAST-LVOS* experiment was designed to further our understanding of the impacts of STT, wildfires, long-range transport from Asia, and regional pollution on air quality in the Las Vegas Valley. The field campaign was carried out between May 17 and June 30, 2017 in Clark County (NV), which includes the greater Las Vegas area (Fig. 1). The measurement campaign consisted of daily lidar and in situ measurements supplemented by aircraft and ozonesonde profiling during the four IOPs (May 23–25, May 31–June 2, June 10–14, and June 28–30). The daily measurements included chemical composition (e.g., CO and O₃) and meteorological parameters (e.g., air temperature and water vapor) recorded with high temporal resolution by instruments installed in a mobile laboratory (Wild et al., 2017) parked on the summit of Angel Peak (36.32°N, 115.57°W, 2682 m above sea level, a.s.l.), the site of the 2013 LVOS field campaign. This mountain-top site, located ~45 km northwest of the Las Vegas City (see Fig. 1), is far from anthropogenic emission sources and mostly receives free tropospheric air at night, but is frequently influenced during the day by air transported from the Las Vegas Valley through upslope flow in late spring and summer (Langford et al., 2015). The Tunable Optical Profiler for Aerosols and oZone (TOPAZ) 3-wavelength mobile differential absorption lidar (DIAL) system, which was previously deployed to Angel Peak during LVOS, was relocated to the North Las Vegas Airport (NLVA, Fig. 1), where it measured 8-minute averaged vertical profiles of O₃ and aerosol backscatter from 27.5 m to ~8 km above ground level (a.g.l.) with an effective vertical resolution (for O₃) ranging from ~10 m near the surface to ~150 m at 500 m a.g.l. and ~900 m at 6 km a.g.l. The aerosol backscatter profiles were retrieved at 7.5 m resolution. TOPAZ was operated daily, but not continuously, throughout the campaign. NOAA also deployed a continuously operating micro-Doppler lidar at NLVA to measure vertical velocities and relative aerosol backscatter throughout the campaign. Boundary layer heights were inferred from the micro-Doppler measurements following the method in Bonin et al. (2018).

The routine in situ and lidar measurements described above were augmented during the four IOPs by ozonesondes launched up to four times per day (30 launches total during the entire campaign) from the Clark County Department of Air Quality Joe Neal monitoring site located ~8 km north-northwest of the NLVA. Aircraft measurements were also conducted by Scientific Aviation to sample O₃, methane (CH₄), water vapor (H₂O), and nitrogen dioxide (NO₂) between NLVA and Big Bear, CA during the IOPs. Readers can refer to our previous studies (Langford et al., 2010; Alvarez II et al., 2011; Langford et al., 2015; Langford et al., 2017; Langford et al., 2019) for detailed descriptions and configurations of the

TOPAZ and the other measurement instruments. The *FAST-LVOS* field campaign is also described in more detail elsewhere (Langford et al., manuscript in preparation).

The *FAST-LVOS* measurements were augmented by hourly surface O₃ measurements from Joe Neal and other regulatory air quality monitoring sites operated by the Clark County Department of Air Quality (Table S1). Surface observations of O₃ from these and other mostly urban sites were obtained from the U.S. Environmental Protection Agency (EPA) Air Quality System (AQS; <https://www.epa.gov/aqs>). We average the AQS measurements into 0.5° × 0.625° grids for a direct comparison with model results (as in Lin et al., 2012a, b). Surface observations from rural sites and more representative of background air were obtained from the EPA Clean Air Status and Trends Network (CASTNet; <https://www.epa.gov/castnet>).

2.2 GFDL-AM4 and GEOS-Chem

Comparisons of key model configurations are shown in Table S2. AM4 is the new generation of the Geophysical Fluid Dynamics Laboratory chemistry-climate model contributing to the Coupled Model Intercomparison Project, Phase 6 (CMIP6). The model employed in this study, a prototype version of AM4.1 (Horowitz et al., 2020), differs from the AM4 configuration described in Zhao et al. (2018a, 2018b) by including 49 vertical levels extending up to 1 Pa (~80 km) and interactive stratosphere-troposphere chemistry and aerosols. Major physical improvements in GFDL-AM4, compared to its predecessor GFDL-AM3 (Donner et al., 2011), include a new double-plume convection scheme with improved representation of convective scavenging of soluble tracers, new mountain drag parametrization, and the updated hydrostatic FV³ cubed-sphere dynamical core (Zhao et al., 2016; Zhao et al., 2018a, b). For tropospheric chemistry, GFDL-AM4 includes improved treatment of photo-oxidation of biogenic VOCs, photolysis rates, heterogeneous chemistry, sulfate and nitrate chemistry, and deposition processes (Mao et al., 2013a; Mao et al., 2013b; Paulot et al., 2016; Li et al., 2016; Paulot et al., 2017), as described in more detail by Schnell et al. (2018). We implement a stratospheric O₃ tracer (O₃Strat) in GFDL-AM4 to track O₃ originating from the stratosphere. The O₃Strat is defined relative to a dynamically varying e90 tropopause (Prather et al., 2011) and is subject to tropospheric chemical loss (in the same manner as odd oxygen of tropospheric origin) and deposition to the surface (Lin et al., 2012a; Lin et al., 2015a). The model is nudged to NCEP reanalysis winds using a height-dependent nudging technique (Lin et al., 2012b). The nudging minimizes the influences of chemistry-climate feedbacks and ensures that the large-scale meteorological conditions are similar to those observed, across the sensitivity simulations. We conduct a suite of AM4 simulations at C192 (~50×50 km²) horizontal resolution for January–June 2017: (1) a BASE

simulation with all emissions included; (2) a sensitivity simulation without anthropogenic emissions over North America (15° – 90° N, 165° – 50° W; NAB); (3) a sensitivity simulation without anthropogenic emissions over the U.S. (USB); (4) a sensitivity simulation without Asian anthropogenic emissions, and (5) a sensitivity simulation without wildfire emissions (see Table S3). The high-resolution BASE and sensitivity simulations for January–June 2017 are initialized from the corresponding nudged C96 ($\sim 100 \times 100 \text{ km}^2$) simulations spanning from 2009 to 2016 (8 years). Compared to the NAB simulation, the USB simulation includes additional contributions from Canadian and Mexican anthropogenic emissions. The USB estimates are now generically defined as “background O₃” and used by the U.S. EPA. Over the WUS, the vertical model resolution ranges from ~ 50 – 200 m near the surface to ~ 1 – 1.5 km near the tropopause and ~ 2 – 3 km in much of the stratosphere.

Goddard Earth Observing System coupled with Chemistry (GEOS-Chem; <http://geos-chem.org>) is a widely used global chemical transport model (CTM) for simulating atmospheric composition and air quality (Bey et al., 2001; Zhang et al., 2011), driven by assimilated meteorological fields from the NASA Global Modeling and Assimilation Office (GMAO). We conduct high-resolution simulations over North America (10° – 70° N, 140° – 40° W), with 0.25° (latitude) $\times 0.3125^{\circ}$ (longitude) horizontal resolution, using a one-way nested-grid version of GEOS-Chem (v11.01) (Wang et al., 2004; Chen et al., 2009) driven by the Goddard Earth Observing System – Forward Processing (GEOS-FP) assimilated meteorological data. The model uses a fully coupled NO_x-Ox-hydrocarbon-aerosol-bromine chemistry mechanism in the troposphere (“Tropchem”), whereas a simplified linearized chemistry mechanism (Linoz) is used in the stratosphere to simulate stratospheric ozone and cross-tropopause ozone fluxes (McLinden et al., 2000). Although GEOS-Chem can also be run with the Universal tropospheric-stratospheric Chemistry eXtension (UCX) mechanism that simulates interactive stratosphere-troposphere chemistry and aerosols (Eastham et al., 2014), this option was not used in the simulations presented in this study due to computational constraints. To further save computational resources, we used a reduced vertical resolution of 47 hybrid eta levels, by combining vertical layers above ~ 80 hPa from the native 72 levels of GEOS-FP. The thickness of model vertical layers over the WUS ranges from ~ 15 – 100 m near the surface to ~ 1 km near the tropopause and in the lower stratosphere. Similar GEOS-Chem simulations with simplified treatments of stratospheric chemistry and dynamics have been previously used to estimate background O₃ for U.S. EPA policy assessments (Zhang et al., 2011; Zhang et al., 2014; Fiore et al., 2014; Guo et al., 2018). Thus, it is important to assess the ability of this model to represent high-background-O₃ events from stratospheric

intrusions. We conduct two nested high-resolution simulations with GEOS-Chem for February–June 2017: BASE and a USB simulation with anthropogenic emissions zeroed out in the U.S. (Table S3). Initial and boundary conditions for chemical fields in the nested-grid simulations were provided by the corresponding BASE and USB GEOS-Chem global simulations at $2^\circ \times 2.5^\circ$ resolution for January–June 2017. Only results for April–June from the nested simulations are analyzed in this study. The three-month spin-up period (January–March) used for GEOS-Chem is relatively short compared to the multi-year GFDL-AM4 simulations, although it should be sufficient given that the lifetime of ozone in the free troposphere is approximately three weeks (e.g., Young et al., 2018).

2.3 Emissions

The anthropogenic emissions used in GFDL-AM4 are modified from the CMIP6 historical emission inventory (Hoesly et al., 2018). The CMIP6 emission inventory does not capture the decreasing trend in anthropogenic NO_x emissions over China after 2011 as inferred from satellite-measured tropospheric NO₂ columns (Liu et al., 2016; Fig. S1). We thus scale CMIP6 NO_x emissions over China after 2011 based on a regional emission inventory developed by Tsinghua University (personal communications with Qiang Zhang at Tsinghua University; Fig. S1). The adjusted NO_x emission trend over China agrees well with the NO₂ trend derived from satellite retrievals. We also reduce NO_x emissions over the EUS (25° – 50° N, 94.5° – 75° W) by 50% following Travis et al. (2016), who suggested that excessive NO_x emissions may be responsible for the common model biases in simulating O₃ over the southeastern U.S. These emission adjustments reduce mean MDA8 O₃ biases in GFDL-AM4 by \sim 5 ppbv in spring and \sim 10 ppbv in summer over the EUS (Fig. S2). The model applies the latest daily-resolving global fire emission inventory from NCAR (FINN) (Wiedinmyer et al., 2011), vertically distributed over six ecosystem-dependent altitude layers from the ground surface to 6 km (Dentener et al., 2006; Lin et al., 2012b). Biogenic isoprene emissions (based on MEGAN; Guenther et al., 2006; Rasmussen et al., 2012), lightning NO_x emissions, dimethyl sulfide, and sea salt emissions are tied to model meteorological fields (Donner et al., 2011; Naik et al., 2013).

For GEOS-Chem, anthropogenic emissions over the United States are scaled from the 2011 U.S. NEI to reflect the conditions in 2017 (<https://www.epa.gov/air-emissions-inventories/air-pollutant-emissions-trends-data>). Similar to AM4, we reduce EUS anthropogenic NO_x emissions in GEOS-Chem by 50% to improve simulated O₃ distributions. Anthropogenic emissions over China are based on the 2010 MIX

emission inventory (Li et al., 2017), with NO_x emissions scaled after 2010 using the same trend as in GFDL-AM4. Biogenic VOC emissions are calculated online with MEGAN (Guenther et al., 2006). Biomass burning emissions are from the FINN inventory but implemented in the lowest model layer. The model calculates lightning NO_x emissions using a monthly climatology of satellite lightning observations coupled to parameterized deep convection (Murray et al., 2012). The calculation of lightning NO_x in this study differs from that in Zhang et al. (2014), who used the U.S. National Lightning Detection Network (NLDN) data to constrain model flash rates.

3 Overall model evaluation

3.1 GFDL-AM4 versus GFDL-AM3

[Figure 2 about here]

We first compare O₃ simulations in AM4 with those from its predecessor, AM3, which has been extensively used in previous studies to estimate background O₃ (Lin et al., 2012a; Lin et al., 2012b; Fiore et al., 2014; Lin et al., 2015a). Figure 2 shows the comparisons of simulated and observed March mean O₃ vertical profiles and mid-tropospheric O₃ seasonal cycles at the Trinidad Head and Boulder ozonesonde sites. Free tropospheric O₃ measured at both sites in March is representative of background conditions, with little influence from U.S. anthropogenic emissions. Thus, we also show O₃ from the NAB simulations with North American anthropogenic emissions zeroed out. As constrained by the availability of AM3 simulations from previous studies, we focus on the 2010–2014 period and compare the NAB estimates as opposed to the USB estimates used in the rest of the paper. Compared with AM3, simulations of free tropospheric O₃ are much improved in AM4. Mean O₃ biases are reduced by 10–25 ppbv in the middle troposphere and 20–65 ppbv in the upper troposphere in AM4, reflecting mostly an improved simulation of background O₃ (Fig. 2a). These improvements are mainly credited to the changes in dynamics/convection schemes in AM4 (Zhao et al., 2018a), according to our sensitivity simulations (not shown). The difference in emissions inventories contribute to some of the O₃ differences but is not the major cause because the largest differences between the two models in simulated free tropospheric O₃ occur during the cold months (November–April) when photochemistry is weak (Fig. 2b).

3.2 GFDL-AM4 versus GEOS-Chem

[Figure 3 about here]

Next, we examine how GFDL-AM4 compares with GEOS-Chem in simulating the mean distribution and the day-to-day variability of total and USB O₃ in the free troposphere (Fig. 3) and at the surface (Fig. 4 and Fig. S3) during *FAST-LVOS*. Comparisons with ozonesondes at Joe Neal show that the total O₃ concentrations below 700 hPa simulated by the two models often bracket the observed values (Fig. 3a). Between 700–300 hPa, GFDL-AM4 better captures the observed mean and day-to-day variability of O₃, as evaluated with the standard deviation. Further comparison with lidar measurements averaged over 3–6 km altitude above Las Vegas shows that total and USB O₃ in GFDL-AM4 exhibits larger day-to-day variability than in GEOS-Chem ($\sigma = 8.1$ ppbv in observations, 8.1 ppbv in AM4, and 6.7 ppbv in GEOS-Chem; Fig. 3c). For mean O₃ levels in the free troposphere, AM4 estimates a 7 ppbv contribution from U.S. anthropogenic emissions (total minus USB), while GEOS-Chem suggests only 3.5 ppbv. The largest discrepancies between the two models occurred on June 11–13 (the blue shaded period in Fig. 3c), which we later attribute to a stratospheric intrusion event (Sect. 4). During this period, AM4 simulates elevated O₃ (70–75 ppbv) broadly consistent with the lidar and sonde measurements, while GEOS-Chem considerably underestimates the observations by 20 ppbv. Consistent with total O₃, USB O₃ in GFDL-AM4 is much higher than GEOS-Chem during this event.

[Figure 4 about here]

Figure 4 shows the times series of observed and simulated surface MDA8 O₃ at four high-elevation sites and one low-elevation site in the region during the study period. Statistics comparing the results at all sites are shown in Table S1. The two models show large differences in simulated total and USB O₃ on days when the O₃Strat tracer in AM4 indicates stratospheric influence (highlighted in blue shading). AM4 O₃Strat indicates frequent STT events during April–June, with MDA8 O₃ exceeding or approaching the current NAAQS of 70 ppbv. Compared with observations, GFDL-AM4 captures the spikes of MDA8 O₃ and elevated USB O₃ during these STT events (e.g., April 23, May 13, and June 11). On these days, GEOS-Chem underestimates observed O₃ by 10–25 ppbv and simulates much lower USB O₃ levels than GFDL-AM4. The two models also differ substantially in total and USB O₃ (14–18 ppbv) on June 22 (yellow shading), with GEOS-Chem overestimating observations at high-elevation sites while GFDL-AM4 underestimates observations at both high- and low-elevation sites. We provide more in-depth analysis of these events in Sect. 4 and identify the possible causes of the model biases.

4 Process-oriented analysis of high-ozone events during *FAST-LVOS*

[Table 1 about here]

We identify ten events with observed MDA8 O₃ exceeding 65 ppbv at multiple sites in the greater Las Vegas area during April–June 2017. Table 1 provides an overview of the events, the dominant source for each event, the surface sites impacted, and the associated analysis figures presented in this article. The attribution is based on a combination of observational and modeling analyses. First, we examine the O₃/CO/H₂O relationships and collocated meteorological measurements from the NOAA/ESRL mobile lab deployed at Angel Peak to provide a first guess on the possible sources of the observed high-O₃ events (Sect. 4.1). Then, we analyze large-scale meteorological fields (e.g., potential vorticity), satellite images (e.g., AIRS CO), and lidar and ozonesonde observations to examine if the transport patterns, the high-O₃ layers, and related tracers are consistent with the key characteristics of a particular source (Sect. 4.2–4.5). Available aerosol backscatter measurements and multi-tracer aircraft profiles are also used to support the attribution (Sect. 4.3 and 4.6). Finally, for each event we examine the spatiotemporal correlations of model simulations of total O₃, background O₃, and its components (e.g., stratospheric ozone tracer), both in the free troposphere and at the surface. For a source to be classified as the dominant driver of an event, O₃ from that source must be elevated sufficiently from its mean baseline value.

4.1 Observed O₃/CO/H₂O relationships

[Figures 5-6 about here]

Relationships between concurrently measured O₃ and CO are useful to identify the possible origins of elevated surface O₃ (Parrish et al., 1998; Herman et al., 1999; Langford et al., 2015). During *FAST-LVOS*, in-situ 1-min measurements at Angel Peak show differences in $\Delta O_3/\Delta CO$ and water vapor content between air plumes during a variety of events (Figs. 5, 6, and S4). Notably, on June 11, O₃ was negatively correlated with CO ($\Delta O_3/\Delta CO = -3.79$). This anti-correlation is distinctly different from the O₃/CO relationships during other periods (e.g., $\Delta O_3/\Delta CO = 0.68\text{--}0.70$ on June 16 or $\Delta O_3/\Delta CO = 1.08$ on June 2). The negative correlation (high O₃ together with low CO) serves as strong evidence of a stratospheric origin of the air masses on June 11, since O₃ is much more abundant in the stratosphere than in the troposphere whereas CO is mostly concentrated within the troposphere where it is directly emitted or chemically formed (Langford et al., 2015). On the contrary, simultaneously elevated O₃ and CO suggest influences by wildfires (e.g., June 22) or anthropogenic (e.g., June 16) pollution (Figs. 6b–d and S4). In particular, exceptionally high CO levels ($\sim 100\text{--}440$ ppbv) on June 22 (Fig. 6e) suggest influences from wildfires. Ozone enhancements were measured by the TOPAZ ozone lidar on June 22 (Sect. 4.3), although the

correlation between CO and O₃ at Angel Peak is not strong. The net production of O₃ by wildfires is highly variable, with many contradictory observations reported in the literature (Jaffe and Wigder, 2012). The amount of O₃ within a given smoke plume varies with distance from the fire and depends on the plume injection height, smoke density, and cloud cover (Faloona et al., 2020).

We gain further insights by examining water vapor concurrently measured at Angel Peak. Air masses from the lower stratosphere are generally dry, whereas wildfire/urban plumes from the boundary layer are relatively moist (Langford et al., 2015). Thus, the dry conditions of the air masses on June 11 support our conclusion that the plume was transported downward from the upper troposphere and lower stratosphere (Fig. 6a). These conditions are in contrast to those of the urban/wildfire plumes transported from the Las Vegas Valley (Fig. 6c–6d). Additionally, we separate the anthropogenic plumes on June 16 into daytime and nighttime conditions because of a diurnal variation of air conditions (relatively dry at night versus wet during daytime; Figs. 6c–d). This analysis further demonstrates that the anthropogenic pollution plume during nighttime is wetter than the stratospheric air on June 11. On June 14 (Fig. 6b), measured O₃ was positively correlated with CO, indicating regional/local pollution influence, but the lower levels of water vapor than those in regional pollution and wildfire plumes suggest that the stratospheric air which reached Angel Peak earlier may have been mixed with local pollution. On June 28 (Fig. 6f), O₃ was positively correlated with CO and the air masses were relatively dry, indicating that the plume was likely from aged pollution transported from Asia or Southern California as opposed to from fresh pollution from the Las Vegas Valley. Identifying the primary source of the high-O₃ events solely based on observations is challenging; additional insights from models are thus needed as we demonstrate below.

4.2 Characteristics of stratospheric intrusion during June 11–14

[Figures 7–8 about here]

Analysis of the 250 hPa potential vorticity and the AM4 model stratospheric O₃ tracer shows significant stratospheric influence on surface O₃ in the SWUS on April 22–23 (Fig. S5), May 13–14 (Fig. S5), and June 11–14 (Figs. 7–8). During these events, surface MDA8 O₃Strat in AM4 was 20–40 ppbv higher than the mean baseline level (15–20 ppbv; see dashed purple lines Fig. 4). Below, we focus on the June 11–14 event, which was the subject of a 4-day *FAST-LVOS* IOP with 60 hours of continuous O₃ lidar profiling and 13 ozonesonde launches, in addition to continuous in situ measurements at Angel Peak.

Deep stratospheric intrusion on June 11–13

Synoptic-scale patterns of potential vorticity (PV) indicate a strong upper-level trough over the northwest U.S. on June 12 (PV = 4–5 PVU in Fig. 7a). The PV pattern displays a “hook-shaped” streamer of air extending from the northern U.S. to the Intermountain West, a typical feature for a STT event (Lin et al., 2012a; Akritidis et al., 2018). This upper-level trough penetrated southeastwardly towards the SWUS, facilitating the descent of stratospheric air masses into the lower troposphere. Ozonesondes launched at Joe Neal on June 12 recorded elevated O₃ levels of 150–270 ppbv at 5–8 km altitude (color-coded circles in Fig. 7b). Consistent with the ozonesonde measurements, GFDL-AM4 shows that O₃-rich stratospheric air masses descended isentropically towards the study region, with simulated O₃ reaching 90 ppbv at ~2 km altitude. For comparison, GEOS-Chem simulates a much weaker and shallower intrusion (Fig. 7b), despite a similar synoptic-scale pattern of potential vorticity at 250 hPa and comparable ozone levels in the UTLS (Fig. S6), suggesting possibly greater numerical diffusion in GEOS-Chem diluting the stratospheric intrusion.

TOPAZ lidar measurements at NLVA vividly characterize the strength and vertical depth of intruding O₃ tongues evolving with time (Fig. 8a). A tongue of high O₃ exceeding 100 ppbv descended to as low as 2–3 km altitude on June 12. GFDL-AM4 captures both the timing and structure of the observed high-O₃ layer and attributes it to a stratospheric origin as supported by the O₃Strat tracer. In contrast, GEOS-Chem substantially underestimates the depth and magnitude of the observed high-O₃ layers in the free troposphere. Zhang et al. (2014) also showed that GEOS-Chem captures the timing of stratospheric intrusions but underestimates their magnitude by a factor of 3.

[Figure 9 about here]

Surface observations show that high MDA8 O₃ exceeding 60 ppbv first emerged on June 11 over Southern Nevada (Fig. 9), consistent with the arrival of stratospheric air masses as inferred from the negative correlation between O₃ and CO measured at Angel Peak (Fig. 6a). Over the next few days, the areas with observed MDA8 O₃ approaching 70 ppbv gradually shifted southward from Nevada and Colorado to Arizona and New Mexico. By June 13, observed surface MDA8 O₃ exceeded 70 ppbv over a large proportion of the SWUS, including Arizona and New Mexico. GFDL-AM4 captures well the observed day-to-day variability of high-O₃ spots over the WUS, although the model overall has high biases. Over the areas where observed MDA8 O₃ levels are 60–75 ppbv, GFDL-AM4 estimates 50–65 ppbv USB O₃.

with simulated O₃Strat 20–40 ppbv higher than its mean baseline level in June. GEOS-Chem has difficulty simulating the observed high-O₃ areas during this event and simulated USB is 15 ppbv lower than AM4 (Fig. 9). These results are consistent with the fact that GEOS-Chem does not capture the structure and magnitude of deep stratospheric intrusions during the period (Figs. 3, 7, and 8).

Mixing of stratospheric ozone with regional pollution on June 14

Stratospheric air masses that penetrate deep into the troposphere can mix with regional anthropogenic pollution and gradually lose their typical stratospheric characteristics (cold and dry air containing low levels of CO), challenging diagnosis of stratospheric impacts based directly on observations (Cooper et al., 2004; Lin et al., 2012b; Trickl et al., 2016). On June 14, O₃ measured at Angel Peak is positively correlated with CO ($\Delta O_3/\Delta CO = 0.75$; Fig. 6b), similar to conditions of anthropogenic pollution on June 16 (Fig. 6c–d). TOPAZ lidar shows elevated O₃ of 70–80 ppbv concentrated within the boundary layer below 3 km altitude (Fig. 8b). These observational data do not provide compelling evidence for stratospheric influence. However, GFDL-AM4 simulates elevated O₃Strat coinciding with the observed and modeled total O₃ enhancements within the PBL, indicating that O₃ from the deep stratospheric intrusion on the previous day may have been mixed with regional anthropogenic pollution to elevate O₃ in the PBL. At the surface (the bottom panel in Fig. 9), AM4 simulates high USB O₃ and elevated O₃Strat (20–40 ppbv above its mean baseline) over Arizona and New Mexico where MDA8 O₃ greater than 70 ppbv was observed. The fact that GEOS-Chem is unable to simulate the ozone enhancements in lidar measurements and at the surface further supports the possible stratospheric influence. This case study demonstrates the value of integrating observational and modeling analysis for the attribution of high-O₃ events over a region with complex O₃ sources.

The extent to which stratospheric intrusions contribute to surface O₃ at low-elevation sites over the WUS is poorly characterized in previous studies. Notably, surface O₃ at three low-elevation (~700–800 m a.s.l.) air quality monitoring sites in Clark County exceeded the current NAAQS level of 70 ppbv on June 14: 74 ppbv at Joe Neal, 73 ppbv at North Las Vegas Airport, and 71 ppbv at Walter Johnson. The number of monitoring sites with O₃ exceedances would have increased to eleven in Clark County if the NAAQS had been lowered to 65 ppbv. While O₃ produced from regional anthropogenic emissions still dominates pollution in the Las Vegas Valley (Fig. S7), our analysis shows that stratospheric intrusions can mix with regional pollution to push surface O₃ above the NAAQS.

4.3 Wildfires on June 22

[Figure 10 about here: Aerosol backscatter]

[Figure 11 about here]

Significant enhancements in aerosol backscatter were observed at 3–6 km altitude above NLVA on June 21–22, indicating the presence of wildfire smoke (Fig. 10a). Under the influence of the wildfire plume, mobile lab measurements at Angel Peak (~3 km altitude) detected elevated CO as high as 440 ppbv in warm, moist air masses (Fig. 6e). The lidar measurements at NLVA on June 22 showed broad O₃ enhancements (80–100 ppb) from the surface to 4 km altitude (Fig. 11a). After 12:00 PDT (19:00 UTC), a deep PBL (3–4 km) developed and O₃ within the PBL was substantially enhanced (> 80 ppbv), likely due to strong O₃ production through reactions between abundant VOCs in the wildfire plumes and NO_x in urban environments (Singh et al., 2012; Gong et al., 2017). Surface MDA8 O₃ exceeded 70 ppbv at multiple sites in the Las Vegas Valley during the event (Table 1). Unfortunately, the synoptic conditions did not trigger an IOP, so there were no aircraft or ozonesonde measurements during this event.

GFDL-AM4 has difficulty simulating the O₃-rich plumes above Clark County on June 22 (Fig. 11a). GEOS-Chem captures the observed high-O₃ layers within the PBL, but overestimates O₃ at 3–6 km altitude (see also Figs. 3b and 11a), likely due to excessive O₃ produced from lightning NO_x over the southern U.S. (Zhang et al., 2011; Zhang et al., 2014). At the surface, total MDA8 O₃ concentrations simulated by the two models bracket the observed values at sites in the Las Vegas area (see yellow shading in Fig. 4) and across the Intermountain West (Fig. 12a). AM4 does not simulate elevated O₃ during this event, while GEOS-Chem simulates elevated total and USB O₃ levels across the entire Southwest region. GEOS-Chem simulations during this wildfire event agree better with the observed MDA8 O₃ enhancements (> 70 ppbv) at Joe Neal (Fig. 4). At the high-elevation sites Angel Peak and Spring Mountain Youth Camp, however, GEOS-Chem overestimates the observed MDA8 O₃ by 10–15 ppbv. Overall, GEOS-Chem seems to be more consistent with observations than GFDL-AM4 during this wildfire event. However, we cannot rule out the possibility that the better agreement between observations and GEOS-Chem simulations during this event may reflect excessive O₃ from lightning NO_x in the model (Zhang et al., 2014).

Meteorological conditions (e.g., temperature and wind fields) on June 22 in the reanalysis data used by GFDL-AM4 and GEOS-Chem are similar over the WUS (not shown). The two models use the same wildfire emissions (FINN) but with different vertical distributions. Fire emissions are distributed between the surface and 6 km altitude in GFDL-AM4 but are placed at the surface level in GEOS-Chem. We conduct several sensitivity simulations with GFDL-AM4 to investigate the causes of the model biases. Placing all fire emissions at the surface in GFDL-AM4 results in ± 5 ppbv differences in modeled MDA8 O₃ on June 22 (Fig. S8). Observations suggested that 40% of NO_x can be converted rapidly to PAN and 20% to HNO₃ in fresh boreal fire plumes over North America (Alvarado et al., 2010). Both models currently treat 100% of wildfire NO_x emissions as NO. We conduct an additional AM4 sensitivity simulation, in which 40% of the wildfire NO_x emissions are released as PAN and 20% as HNO₃. This treatment results in ± 2 ppbv differences in simulated monthly mean MDA8 O₃ during an active wildfire season (August 2012; Fig. S9). Overall, these changes do not substantially improve simulated O₃ on June 22. Future efforts are needed to investigate the ability of current models to simulate O₃ formations in fire plumes (Jaffe et al., 2018).

4.4 Regional and local anthropogenic pollution events

[Figure 12 about here]

Regional and local anthropogenic emissions were important sources of elevated O₃ in Clark County during *FAST-LVOS*, contributing to three out of ten observed high-O₃ events above 65 ppbv during April–June 2017 (Table 1). Below, we focus on the June 16 event when severe O₃ pollution with MDA8 O₃ exceeding 70 ppbv occurred over California, Arizona, parts of Nevada, and New Mexico. Analysis for the June 2 and June 29–30 pollution events are shown in the supplemental material (Figs. S4, S10, and S11). The TOPAZ lidar measurements on June 16 show elevated O₃ of 55–90 ppbv in the 4-km-deep PBL (Fig. 11b). However, this event did not trigger an IOP, so ozonesonde and aircraft measurements are unavailable. Both GFDL-AM4 and GEOS-Chem capture the buildup of O₃ pollution in the PBL on June 16 (Fig. 11b). Both models show boundary layer enhancements of total O₃ but not of USB O₃ (Fig. 11b), indicating that regional or local anthropogenic emissions are the primary source of observed O₃ enhancements. Similar to June 16, GEOS-Chem clearly shows enhancements in total O₃ in the PBL but not in USB O₃ on June 2 and June 29–30 (Fig. S10). The model attribution to U.S. anthropogenic emissions is consistent with the positive correlation between O₃ and CO measured at Angel Peak on June 16 (Fig. 6c–6d), June 2, and

June 29–30 (Fig. S4). It is noteworthy that, with its higher horizontal resolution, GEOS-Chem better resolves the structure of the O₃ plumes as observed by TOPAZ lidar for all the three pollution events. At the surface, both models capture the large-scale MDA8 O₃ enhancements across the SWUS on June 16 (Fig. 12b). The surface O₃ enhancements on June 2 and June 29–30 are relatively localized in Southern California and the Las Vegas area (Fig. S11), and both models have difficulty simulating the observed peak MDA8 values (Fig. 4).

4.5 Long-range transport of Asian pollution on May 20–24

[Figures 13-15 about here]

During May 20–24, long-range transport of Asian pollution toward the WUS was observed via large-scale CO column observations with Atmospheric Infrared Sounder (AIRS) on NASA's Aqua satellite (Fig. 13a). These Asian plumes traveled eastward across the Pacific for several days, reaching the west coast of the U.S. on May 23 during the first *FAST-LVOS* IOP (May 23–25). The lidar measurements at NLVA on May 24 clearly showed high-O₃ plumes (> 70 ppbv) concentrated within the layers of 1–4 km and 6–8 km altitude above the Las Vegas Valley throughout the day (Fig. 14a). Both GFDL-AM4 and GEOS-Chem capture the observed O₃-rich plumes at surface–4 km and 6–8 km altitude above Clark County during this event. Elevated O₃ at 6–8 km altitude reflects the long-range transport from Asia, as supported by concurrent enhancements in total and USB O₃ in both models and by the large difference in O₃ between the AM4 BASE simulation and the sensitivity simulation with Asian anthropogenic emissions zeroed out. Elevated O₃ at 1–4 km altitude appears to be influenced by a residual pollution layer from the previous day; this plume was later mixed into the growing PBL (up to 4 km altitude), elevating MDA8 O₃ in surface air on May 24. Further supporting the impact from regional or local pollution below 4 km altitude, both models simulate much larger enhancements in total O₃ (70–90 ppbv) than in USB O₃ (~50 ppbv).

On May 24, MDA8 O₃ approached or exceeded the 70-ppbv NAAQS at multiple sites in California, Idaho, Wyoming, and Nevada (Fig. 15a), likely reflecting the combined influence of regional pollution and long-range transport of Asian pollution. MDA8 O₃ at four surface sites in Clark County was above 65 ppbv. More exceedances would have occurred if the level for the NAAQS were lowered to 65 ppbv. In parts of Idaho, Wyoming, and California where observed MDA8 O₃ was higher than 60 ppbv, the contribution of Asian anthropogenic emissions as estimated by GFDL-AM4 was 8–15 ppbv (Fig. 15a), much higher than the springtime average contribution of ~5 ppbv estimated by previous studies (e.g., Lin et al., 2012b),

supporting the episodic influence from Asian pollution during this event. At several high-elevation sites in California such as Arden Peak (72 ppbv) and Yosemite National Park (70 ppbv), where observed MDA8 O₃ exceeds the NAAQS level, the contribution of Asian pollution is approximately 9 ppbv. Ozone produced from regional and local anthropogenic emissions dominates the observed MDA8 O₃ above 70 ppbv in the Central Valley of California.

4.6 An unattributed event: June 28

The lidar measurements from June 28 show a fine-scale structure with a narrow O₃ layer exceeding 100 ppbv at 3–4 km altitude during 08:00–14:00 PDT (15:00–21:00 UTC shown in Fig. 14b). An ozonesonde launched at 12:00 PDT also detected a high-O₃ layer (~115 ppbv) between 3.5 and 4 km altitude (not shown). This high-O₃ filament appears to descend and mix into the PBL after 14:00 PDT (21:00 UTC), contributing to elevated O₃ within the PBL in the afternoon. Both models are unable to represent this fine-scale transport event, possibly due to diffusive mixing of the narrow layer (Fig. 14b). We, therefore, focus on available airborne and in situ measurements to investigate the origin of this fine-scale O₃ filament.

Our examinations of large-scale satellite CO column measurements reveal a migration during June 23–27 of high-CO plumes from Asia that arrived at the west coast of the U.S. on June 27 (Fig. 13b). GFDL-AM4 estimates 5–6 ppbv contributions from Asian pollution over the WUS on June 28 (Figs. 15b), which do not represent a significant enhancement above the mean Asian contribution. Aircraft measurements above the Las Vegas Valley in the late morning showed collocated enhancements in CH₄ and O₃ coincident with low free-tropospheric water vapor values at 3–4 km altitude (Fig. 10b). In-situ measurements at Angel Peak show concurrent increases in CO and O₃ coincident with relatively dry conditions that are consistent with transported Asian pollution, but these increases did not appear until several hours after the fine-scale filament was entrained by the mixed layer (Fig. 6f). These observations indicate that the O₃-rich plume appears to be unrelated to stratospheric intrusions. Aerosol backscatter measurements at NLVA show only a slight enhancement in backscatter within the elevated O₃ layer on June 28, in contrast to the thick smoke observed on June 22 when the Las Vegas Valley was influenced by fresh wildfires (Fig. 10). HYSPLIT and FLEXPART analyses presented in Langford et al. (in preparation) suggest a possible connection to the Schaeffer Fire (https://en.wikipedia.org/wiki/Schaeffer_Fire) in the Sequoia National Forest in California. Another possible source is the fine-scale lofting of pollution from Southern California followed by transport into the free troposphere over Las Vegas (Langford et al., 2010). This event further

demonstrates the complexity of O₃ sources in the SWUS. We recommend measurements of atmospheric compounds like acetonitrile (CH₃CN, abundant in fire plumes) and methyl chloride (CH₃Cl, abundant in Asian pollution) (Holzinger et al., 1999; Barletta et al., 2009) via aircraft and in situ platforms in future field campaigns in the region to help identify the sources of such high-O₃ filaments.

5 Comparison of background ozone simulated with GFDL-AM4 and GEOS-Chem

[Figure 16 about here]

Here, we summarize the differences in total and background O₃ between the two models over the WUS. GFDL-AM4 and GEOS-Chem differ in their spatial distributions and magnitudes of April–June mean USB O₃ at the surface and in the free troposphere over the U.S. (Fig. 16). USB O₃ in GFDL-AM4 peaks over the high-elevation Intermountain West at the surface (45–55 ppbv) and over the northern U.S. in the free troposphere (3–6 km altitude; 50–65 ppbv) due to the influence of STT. In comparison, GEOS-Chem simulates higher USB O₃ levels in southwestern states (e.g., Texas), both at the surface (45–50 ppbv) and at 3–6 km altitude (55–65 ppbv), likely due to excessive lightning NO_x during early summer (Zhang et al., 2011; Zhang et al., 2014). These discrepancies in USB between the two models likely reflect that GFDL-AM4 simulates stronger STT influences over the WUS while it produces less O₃ from weaker lightning NO_x emissions in the free troposphere over the southern U.S. than GEOS-Chem (Fiore et al., 2014). Despite a quantitative disparity, both models simulate higher USB O₃ levels over the WUS (45–55 ppbv in GFDL-AM4 and 35–45 ppbv in GEOS-Chem) than over the EUS at the surface (Fig. 16a). Our USB O₃ estimates with GEOS-Chem are generally consistent with the estimates in previous studies using GEOS-Chem or regional models driven by GEOS-Chem boundary conditions (Zhang et al., 2011; Emery et al., 2012; Dolwick et al., 2015; Guo et al., 2018). In contrast to NAB O₃ estimates in earlier studies by zeroing out North American anthropogenic emissions (Zhang et al., 2011; Lin et al., 2012a; Fiore et al., 2014; Zhang et al., 2014), USB O₃ estimates in our study include the additional contribution from Canadian and Mexican emissions. USB O₃ at Clark County sites is ~4 ppbv greater than NAB O₃ in GFDL-AM4 (Table S4). We also find that NAB O₃ estimated with the new GFDL-AM4 model is ~5 ppbv lower than the NAB estimates by its predecessor GFDL-AM3 (Lin et al., 2012a) for the WUS during March–April (Fig. S13), consistent with an improved simulation of free tropospheric ozone in AM4 during spring (Fig. 2). During early summer, the NAB O₃ levels estimated by AM3 and AM4 are similar (Fig. S13).

[Figure 17 about here]

We further compare simulated surface MDA8 O₃ against observations at 12 high-elevation sites (> 1500 m altitude; including 11 CASTNet sites and Angel Peak; see Table S1 and black circles in Fig. 1) in the WUS (Fig. 17). The observed high-MDA8-O₃ events above 65 ppbv at these high-elevation sites are generally associated with enhanced background O₃ in both models (USB O₃ = 50–60 ppbv in GFDL-AM4 and 45–55 ppbv in GEOS-Chem; Fig. 17a). Stratospheric intrusions are an important source of the observed events above 70 ppbv (Fig. S14), as suggested by GFDL-AM4, which better captures these high-O₃ events influenced by elevated background O₃ contributions, whereas GEOS-Chem underestimates these extreme events. For mean MDA8 O₃ at these sites, GFDL-AM4 is biased high by 3 ppbv while GEOS-Chem is biased low by 5 ppbv. A recent study by Lin et al. (2019) found that an improved treatment of ozone dry deposition can reduce mean springtime ozone biases in GFDL-AM4 by 5 ppbv. Mean USB O₃ simulated with GFDL-AM4 is 51.4 ± 7.8 ppbv at WUS sites, higher than that in GEOS-Chem (45.7 ± 5.7 ppbv; Fig. 17b). Probability distributions show that GFDL-AM4 simulates a wider range of total and USB O₃ than GEOS-Chem, reflecting relative skill in capturing the day-to-day variability of O₃.

Tables S4 and S5 report year-to-year variability in the percentage of site-days with springtime MDA8 O₃ above 70 ppbv (or 65 ppbv) and simulated USB levels during 2010–2017. The percentage of site-days with MDA8 O₃ above 70 ppbv during April–June 2017 is 0.9% from observations at CASTNet sites, 2.0% from GFDL-AM4, and 0.1% from GEOS-Chem. GFDL-AM4 captures some aspects of the observed year-to-year variability despite mean-state biases. For example, the observed percentage of site-days with MDA8 O₃ above 70 ppbv at CASTNet sites is highest (9.4%) in April–June 2012, compared to $3.1 \pm 3.2\%$ for the 2010–2017 average. The corresponding statistics from GFDL-AM4 are 7.7% for 2012 and $4.0 \pm 2.9\%$ for the 2010–2017 average. The May–June mean USB MDA8 O₃ in GFDL-AM4 at Clark County sites are 50.9 ppbv in 2017, 55.3 ppbv in 2012, and 52.3 ± 2.0 ppbv for the 2010–2017 average. Supporting the conclusions of Lin et al. (2015a), these results indicate that background O₃, particularly the stratospheric influence, is an important source of the observed year-to-year variability in high-O₃ events over the WUS during spring.

6 Discussion and Conclusions

Through a process-oriented analysis of intensive measurements from the 2017 *FAST-LVOS* field campaign and high-resolution simulations with two global models (GFDL-AM4 and GEOS-Chem), we

study the sources of observed MDA8 O₃ above 65 ppbv in the SWUS. Attribution of each event to a specific source is sometimes challenging, despite an integrated analysis of multi-tracer, multi-platform observations and model simulations. We identify the high-O₃ events associated with stratospheric intrusions (April 22–23, May 13–14, and June 11–13), mixing of local pollution and transported stratospheric O₃ (June 14), regional or local anthropogenic pollution (June 2, June 16, and June 29–30), wildfires (June 22), and mixing of Asian pollution with regional pollution (May 24). We also discuss an event (June 28) likely resulting from the fine-scale transport of fire plumes or pollution from Southern California, although a solid attribution for this event is challenging based on available data.

During the June 11–13 deep stratospheric intrusion event, the NOAA mobile lab measurements at Angel Peak show a sharp increase in O₃ coinciding with a decrease in CO and water vapor, a marker for air of stratospheric origin. These characteristics are in contrast to the concurrent increases in O₃ and CO in humid, warm urban plumes and wildfires plumes transported from the Las Vegas Valley. The observed O₃/CO/H₂O relationships can provide a useful first indication of high-O₃ events influenced directly by a deep intrusion. However, once transported stratospheric O₃ is mixed into regional pollution, model diagnostic tracers are needed to quantify the stratospheric impact. For instance, on June 14, observations at Angel Peak show positive O₃/CO correlations while O₃Strat in GFDL-AM4 shows 20–30 ppbv enhancements above its mean level at Angel Peak and at surface sites across the SWUS where the observed and simulated total MDA8 O₃ concentrations were above 70 ppbv.

GFDL-AM4 and GEOS-Chem differ significantly in simulating stratosphere-to-troposphere transport events, affecting their ability to simulate USB mean levels and extreme events. During the June 11–14 STT event, GFDL-AM4 captures the key characteristics of deep stratospheric intrusions, consistent with lidar profiles and ozonesondes, whereas GEOS-Chem with simplified stratospheric chemistry and dynamics has difficulty simulating the observed features. At the surface, on days when observed MDA8 O₃ exceeds 65 ppbv and AM4 O₃Strat is 20–40 ppbv above its mean baseline level, AM4 simulates 15–20 ppbv greater USB O₃ than GEOS-Chem (Figs. 4 and 9). During these STT events, total MDA8 O₃ abundances simulated by the two models often bracket the observed values, as noted previously by Fiore et al. (2014). The *FAST*-LVOS analysis, combined with our earlier multi-year studies (Lin et al. 2012a; Lin et al., 2015a), indicate that GFDL AM3/AM4 with nudged meteorology captures the timing and locations of the observed O₃ enhancements in surface air and aloft during STT events, and is thus useful for screening of exceptional events due to STT. Considering the high biases of total MDA8 O₃ in

AM3/AM4 during some STT events, we recommend bias correction to simulated USB O₃, such as the approach used by Lin et al. (2012a). For the future application of GEOS-Chem for USB estimates, we recommend the version with the Universal tropospheric-stratospheric Chemistry eXtension (UCX) mechanism (Eastham et al., 2014) and process-oriented evaluation using daily ozonesondes and lidar profiles.

The two models also differ substantially in total and background O₃ simulations during the June 22 wildfire event. GEOS-Chem captures the broad O₃ enhancement in lidar observations, but overestimates surface MDA8 O₃ at some sites during this event. It remains unclear whether the higher USB O₃ simulated by GEOS-Chem during this event is from greater O₃ produced from wildfire emissions or excessive lightning NO_x emissions in the model. Although GFDL-AM3 captures the observed interannual variability in O₃ enhancements from large-scale wildfires over the WUS (Lin et al., 2017), GFDL-AM4 has difficulty simulating the observed O₃ enhancements during the relatively small-scale wildfire event on June 22. Sensitivity simulations with fire emissions constrained at the surface or with part of fire NO_x emissions emitted as PAN and HNO₃ do not substantially improve simulated O₃ on June 22. Wildfires typically occur under hot, dry conditions, which also enable the buildup of O₃ produced from regional anthropogenic emissions, complicating an unambiguous attribution of the high-O₃ events solely based on observations. Screening of exceptional events due to wildfire emissions remains a serious challenge.

The multi-model approach tied closely to intensive measurements provides insights into the capability of models to simulate background O₃ and harnesses the strengths of individual models to characterize the sources of high-O₃ events. Stratospheric intrusions, Asian pollution, and wildfires are important sources of the observed high-O₃ events above 65 ppbv in the SWUS, although uncertainties remain in the quantitative attribution. Surface ozone in China continues to increase despite regional NO_x emission controls in recent years (Liu et al., 2016; Li et al., 2019; Sun et al., 2016), contributing to increased background O₃. Furthermore, the increasing frequency of wildfires under a warming climate (e.g., Westerling et al., 2006; Dennison et al., 2014) and growing global methane levels (e.g., West et al., 2006; Morgenstern et al., 2013) may foster higher background O₃ levels in the coming decades (Lin et al., 2017). These increasing background O₃ sources, together with year-to-year variability in stratospheric influence (Lin et al., 2015a), will leave little margin for O₃ produced from local and regional emissions, posing challenges to achieving a potentially tightened O₃ NAAQS in the SWUS.

Data availability. Model simulations presented in this manuscript are available upon request to the corresponding author (Meiyun.Lin@noaa.gov). Field measurements during *FAST-LVOS* are available at <https://www.esrl.noaa.gov/csd/projects/FASTlvos>.

Author contributions. MYL conceived this study and designed the model experiments; LZ performed the GFDL-AM4 simulations and all analysis under the supervision of MYL; EK and YXW conducted the GEOS-Chem simulations; LWH and YXW assisted in the interpretation of model results; AOL, CJS, RJA, IP, PC, JP, TBR, SSB, ZCJD, GK, and SC carried out field measurements. LZ and MYL wrote the article with inputs from all coauthors.

Competing interests. The authors declare that they have no conflict of interest.

Disclaimer. The statements, findings, and conclusions are those of the author(s) and should not be construed as the views of the agencies.

Acknowledgements. This work was funded by the Clark County Department of Air Quality (CCDAQ) under contracts CBE 604279-16 (Princeton University), CBE 604318-16 (NOAA ESRL), and CBE 604380-17 (Scientific Aviation). MYL and LZ were also supported by Princeton University's Cooperative Institute for Modeling the Earth Science (CIMES) under awards NA14OAR4320106 and NA18OAR4320123 from the National Oceanic and Atmospheric Administration, U.S. Department of Commerce. We are grateful to Zheng Li (CCDAQ), Songmiao Fan (GFDL) and Yuanyu Xie (Princeton University) for helpful discussions and suggestions. We thank Qiang Zhang (Tsinghua University) for providing trends of anthropogenic NO_x emissions in China and Christine Wiedinmyer (University of Colorado) for the 2017 FINN emission data.

References

Akritidis, D., Katragkou, E., Zanis, P., Pytharoulis, I., Melas, D., Flemming, J., Inness, A., Clark, H., Plu, M., and Eskes, H.: A deep stratosphere-to-troposphere ozone transport event over Europe simulated in CAMS global and regional forecast systems: analysis and evaluation, *Atmos. Chem. Phys.*, 18, 15515-15534, <https://doi.org/10.5194/acp-18-15515-2018>, 2018.

Alvarado, M. J., Logan, J. A., Mao, J., Apel, E., Riemer, D., Blake, D., Cohen, R. C., Min, K. E., Perring, A. E., Browne, E. C., Wooldridge, P. J., Diskin, G. S., Sachse, G. W., Fuelberg, H., Sessions, W. R., Harrigan, D. L., Huey, G., Liao, J., Case-Hanks, A., Jimenez, J. L., Cubison, M. J., Vay, S. A., Weinheimer, A. J., Knapp, D. J., Montzka, D. D., Flocke, F. M., Pollack, I. B., Wennberg, P. O., Kurten, A., Crounse, J., Clair, J. M. S., Wisthaler, A., Mikoviny, T., Yantosca, R. M., Carouge, C. C.,

and Le Sager, P.: Nitrogen oxides and PAN in plumes from boreal fires during ARCTAS-B and their impact on ozone: an integrated analysis of aircraft and satellite observations, *Atmos. Chem. Phys.*, 10, 9739-9760, <https://doi.org/10.5194/acp-10-9739-2010>, 2010.

Alvarez II, R. J., Senff, C. J., Langford, A. O., Weickmann, A. M., Law, D. C., Machol, J. L., Merritt, D. A., Marchbanks, R. D., Sandberg, S. P., Brewer, W. A., Hardesty, R. M., and Banta, R. M.: Development and Application of a Compact, Tunable, Solid-State Airborne Ozone Lidar System for Boundary Layer Profiling, *Journal of Atmospheric and Oceanic Technology*, 28, 1258-1272, <https://doi.org/10.1175/jtech-d-10-05044.1>, 2011.

Barletta, B., Meinardi, S., Simpson, I. J., Atlas, E. L., Beyersdorf, A. J., Baker, A. K., Blake, N. J., Yang, M., Midyett, J. R., Novak, B. J., McKeachie, R. J., Fuelberg, H. E., Sachse, G. W., Avery, M. A., Campos, T., Weinheimer, A. J., Rowland, F. S., and Blake, D. R.: Characterization of volatile organic compounds (VOCs) in Asian and north American pollution plumes during INTEX-B: identification of specific Chinese air mass tracers, *Atmos. Chem. Phys.*, 9, 5371-5388, <https://doi.org/10.5194/acp-9-5371-2009>, 2009.

Baylon, P. M., Jaffe, D. A., Pierce, R. B., and Gustin, M. S.: Interannual Variability in Baseline Ozone and Its Relationship to Surface Ozone in the Western U.S, *Environ. Sci. Technol.*, 50, 2994-3001, <https://doi.org/10.1021/acs.est.6b00219>, 2016.

Bey, I., Jacob, D. J., Yantosca, R. M., Logan, J. A., Field, B. D., Fiore, A. M., Li, Q., Liu, H. Y., Mickley, L. J., and Schultz, M. G.: Global modeling of tropospheric chemistry with assimilated meteorology: Model description and evaluation, *J. Geophys. Res.-Atmos.*, 106, 23073-23095, <https://doi.org/10.1029/2001JD000807>, 2001.

Bonin, T. A., Carroll, B. J., Hardesty, R. M., Brewer, W. A., Hajny, K., Salmon, O. E., and Shepson, P. B.: Doppler Lidar Observations of the Mixing Height in Indianapolis Using an Automated Composite Fuzzy Logic Approach, *Journal of Atmospheric and Oceanic Technology*, 35, 473-490, <https://doi.org/10.1175/jtech-d-17-0159.1>, 2018.

Chen, D., Wang, Y., McElroy, M. B., He, K., Yantosca, R. M., and Le Sager, P.: Regional CO pollution and export in China simulated by the high-resolution nested-grid GEOS-Chem model, *Atmos. Chem. Phys.*, 9, 3825-3839, <https://doi.org/10.5194/acp-9-3825-2009>, 2009.

Cooper, O., Forster, C., Parrish, D., Dunlea, E., Hübner, G., Fehsenfeld, F., Holloway, J., Oltmans, S., Johnson, B., Wimmers, A., and Horowitz, L.: On the life cycle of a stratospheric intrusion and its dispersion into polluted warm conveyor belts, *J. Geophys. Res.-Atmos.*, 109, <https://doi.org/10.1029/2003JD004006>, 2004.

Dennison, P. E., Brewer, S. C., Arnold, J. D., and Moritz, M. A.: Large wildfire trends in the western United States, 1984–2011, *Geophys. Res. Lett.*, 41, 2928-2933, <https://doi.org/10.1002/2014gl059576>, 2014.

Dentener, F., Kinne, S., Bond, T., Boucher, O., Cofala, J., Generoso, S., Ginoux, P., Gong, S., Hoelzemann, J. J., Ito, A., Marelli, L., Penner, J. E., Putaud, J. P., Textor, C., Schulz, M., van der Werf, G. R., and Wilson, J.: Emissions of primary aerosol and precursor gases in the years 2000 and 1750 prescribed data-sets for AeroCom, *Atmos. Chem. Phys.*, 6, 4321-4344, <https://doi.org/10.5194/acp-6-4321-2006>, 2006.

Dolwick, P., Akhtar, F., Baker, K. R., Possiel, N., Simon, H., and Tonnesen, G.: Comparison of background ozone estimates over the western United States based on two separate model methodologies, *Atmos. Environ.*, 109, 282-296, <https://doi.org/10.1016/j.atmosenv.2015.01.005>, 2015.

Donner, L. J., Wyman, B. L., Hemler, R. S., Horowitz, L. W., Ming, Y., Zhao, M., Golaz, J.-C., Ginoux, P., Lin, S.-J., Schwarzkopf, M. D., Austin, J., Alaka, G., Cooke, W. F., Delworth, T. L., Freidenreich,

S. M., Gordon, C. T., Griffies, S. M., Held, I. M., Hurlin, W. J., Klein, S. A., Knutson, T. R., Langenhorst, A. R., Lee, H.-C., Lin, Y., Magi, B. I., Malyshev, S. L., Milly, P. C. D., Naik, V., Nath, M. J., Pincus, R., Ploshay, J. J., Ramaswamy, V., Seman, C. J., Shevliakova, E., Sirutis, J. J., Stern, W. F., Stouffer, R. J., Wilson, R. J., Winton, M., Wittenberg, A. T., and Zeng, F.: The Dynamical Core, Physical Parameterizations, and Basic Simulation Characteristics of the Atmospheric Component AM3 of the GFDL Global Coupled Model CM3, *J. Climate*, 24, 3484-3519, <https://doi.org/10.1175/2011jcli3955.1>, 2011.

Eastham, S. D., Weisenstein, D. K., and Barrett, S. R. H.: Development and evaluation of the unified tropospheric–stratospheric chemistry extension (UCX) for the global chemistry-transport model GEOS-Chem, *Atmos. Environ.*, 89, 52-63, <https://doi.org/10.1016/j.atmosenv.2014.02.001>, 2014.

Emery, C., Jung, J., Downey, N., Johnson, J., Jimenez, M., Yarwood, G., and Morris, R.: Regional and global modeling estimates of policy relevant background ozone over the United States, *Atmos. Environ.*, 47, 206-217, <https://doi.org/10.1016/j.atmosenv.2011.11.012>, 2012.

Faloona, I. C., Chiao, S., Eiserloh, A. J., II, R. J. A., Kirgis, G., Langford, A. O., Senff, C. J., Caputi, D., Hu, A., Iraci, L. T., Yates, E. L., Marrero, J. E., Ryoo, J.-M., Conley, S., Tanrikulu, S., Xu, J., and Kuwayama, T.: The California Baseline Ozone Transport Study (CABOTS), *B. Am. Meteor. Soc.*, 101, E427-E445, <https://doi.org/10.1175/bams-d-18-0302.1>, 2020.

Fiore, A. M., Oberman, J. T., Lin, M. Y., Zhang, L., Clifton, O. E., Jacob, D. J., Naik, V., Horowitz, L. W., Pinto, J. P., and Milly, G. P.: Estimating North American background ozone in U.S. surface air with two independent global models: Variability, uncertainties, and recommendations, *Atmos. Environ.*, 96, 284-300, <https://doi.org/10.1016/j.atmosenv.2014.07.045>, 2014.

Gong, X., Kaulfus, A., Nair, U., and Jaffe, D. A.: Quantifying O₃ Impacts in Urban Areas Due to Wildfires Using a Generalized Additive Model, *Environ. Sci. Technol.*, 51, 13216-13223, <https://doi.org/10.1021/acs.est.7b03130>, 2017.

Guenther, A., Karl, T., Harley, P., Wiedinmyer, C., Palmer, P. I., and Geron, C.: Estimates of global terrestrial isoprene emissions using MEGAN (Model of Emissions of Gases and Aerosols from Nature), *Atmos. Chem. Phys.*, 6, 3181-3210, <https://doi.org/10.5194/acp-6-3181-2006>, 2006.

Guo, J. J., Fiore, A. M., Murray, L. T., Jaffe, D. A., Schnell, J. L., Moore, C. T., and Milly, G. P.: Average versus high surface ozone levels over the continental USA: model bias, background influences, and interannual variability, *Atmos. Chem. Phys.*, 18, 12123-12140, <https://doi.org/10.5194/acp-18-12123-2018>, 2018.

Herman, R. L., Webster, C. R., May, R. D., Scott, D. C., Hu, H., Moyer, E. J., Wennberg, P. O., Hanisco, T. F., Lanzendorf, E. J., Salawitch, R. J., Yung, Y. L., Margitan, J. J., and Bui, T. P.: Measurements of CO in the upper troposphere and lower stratosphere, *Chemosphere - Global Change Science*, 1, 173-183, [https://doi.org/10.1016/S1465-9972\(99\)00008-2](https://doi.org/10.1016/S1465-9972(99)00008-2), 1999.

Hoesly, R. M., Smith, S. J., Feng, L., Klimont, Z., Janssens-Maenhout, G., Pitkanen, T., Seibert, J. J., Vu, L., Andres, R. J., Bolt, R. M., Bond, T. C., Dawidowski, L., Kholod, N., Kurokawa, J. I., Li, M., Liu, L., Lu, Z., Moura, M. C. P., O'Rourke, P. R., and Zhang, Q.: Historical (1750–2014) anthropogenic emissions of reactive gases and aerosols from the Community Emissions Data System (CEDS), *Geosci. Model Dev.*, 11, 369-408, <https://doi.org/10.5194/gmd-11-369-2018>, 2018.

Holzinger, R., Warneke, C., Hansel, A., Jordan, A., Lindinger, W., Scharfffe, D. H., Schade, G., and Crutzen, P. J.: Biomass burning as a source of formaldehyde, acetaldehyde, methanol, acetone, acetonitrile, and hydrogen cyanide, *Geophys. Res. Lett.*, 26, 1161-1164, <https://doi.org/10.1029/1999gl900156>, 1999.

Horowitz, L. W., Naik, V., Paulot, F., Ginoux, P. A., Dunne, J. P., Mao, J., Schnell, J., Chen, X., He, J., Lin, M., Lin, P., Malyshev, S., P., D., Shevliakova, E., and Zhao, M.: The GFDL Global

Atmospheric Chemistry-Climate Model AM4.1: Model Description and Simulation Characteristics, *J. Adv. Model. Earth Syst.*, submitted, 2020.

Jacob, D. J., Logan, J. A., and Murti, P. P.: Effect of rising Asian emissions on surface ozone in the United States, *Geophys. Res. Lett.*, 26, 2175-2178, <https://doi.org/10.1029/1999GL900450>, 1999.

Jaffe, D. A., and Wigder, N. L.: Ozone production from wildfires: A critical review, *Atmos. Environ.*, 51, 1-10, <https://doi.org/10.1016/j.atmosenv.2011.11.063>, 2012.

Jaffe, D. A., Wigder, N., Downey, N., Pfister, G., Boynard, A., and Reid, S. B.: Impact of Wildfires on Ozone Exceptional Events in the Western U.S, *Environ. Sci. Technol.*, 47, 11065-11072, <https://doi.org/10.1021/es402164f>, 2013.

Jaffe, D. A., Cooper, O. R., Fiore, A. M., Henderson, B. H., Tonneson, G. S., Russell, A. G., Henze, D. K., Langford, A. O., Lin, M., and Moore, T.: Scientific assessment of background ozone over the U.S.: Implications for air quality management, *Elementa: Science of the Anthropocene*, 6(1), <http://doi.org/10.1525/elementa.309>, 2018.

Langford, A. O., Aikin, K. C., Eubank, C. S., and Williams, E. J.: Stratospheric contribution to high surface ozone in Colorado during springtime, *Geophys. Res. Lett.*, 36, L12801, <https://doi.org/10.1029/2009GL038367>, 2009.

Langford, A. O., Senff, C. J., Alvarez, R. J., Banta, R. M., and Hardesty, R. M.: Long-range transport of ozone from the Los Angeles Basin: A case study, *Geophys. Res. Lett.*, 37, <https://doi.org/10.1029/2010GL042507>, 2010.

Langford, A. O., Brioude, J., Cooper, O. R., Senff, C. J., Alvarez, R. J., Hardesty, R. M., Johnson, B. J., and Oltmans, S. J.: Stratospheric influence on surface ozone in the Los Angeles area during late spring and early summer of 2010, *J. Geophys. Res.-Atmos.*, 117, <https://doi.org/10.1029/2011JD016766>, 2012.

Langford, A. O., Senff, C. J., Alvarez, R. J., Brioude, J., Cooper, O. R., Holloway, J. S., Lin, M. Y., Marchbanks, R. D., Pierce, R. B., Sandberg, S. P., Weickmann, A. M., and Williams, E. J.: An overview of the 2013 Las Vegas Ozone Study (LVOS): Impact of stratospheric intrusions and long-range transport on surface air quality, *Atmos. Environ.*, 109, 305-322, <https://doi.org/10.1016/j.atmosenv.2014.08.040>, 2015.

Langford, A. O., Alvarez II, R. J., Brioude, J., Fine, R., Gustin, M. S., Lin, M. Y., Marchbanks, R. D., Pierce, R. B., Sandberg, S. P., Senff, C. J., Weickmann, A. M., and Williams, E. J.: Entrainment of stratospheric air and Asian pollution by the convective boundary layer in the southwestern U.S, *J. Geophys. Res.-Atmos.*, 122, 1312-1337, <https://doi.org/10.1002/2016JD025987>, 2017.

Langford, A. O., Alvarez II, R. J., Kirgis, G., Senff, C. J., Caputi, D., Conley, S. A., Faloona, I. C., Iraci, L. T., Marrero, J. E., McNamara, M. E., Ryoo, J. M., and Yates, E. L.: Intercomparison of lidar, aircraft, and surface ozone measurements in the San Joaquin Valley during the California Baseline Ozone Transport Study (CABOTS), *Atmos. Meas. Tech.*, 12, 1889-1904, <https://doi.org/10.5194/amt-12-1889-2019>, 2019.

Li, J., Mao, J., Min, K.-E., Washenfelder, R. A., Brown, S. S., Kaiser, J., Keutsch, F. N., Volkamer, R., Wolfe, G. M., Hanisco, T. F., Pollack, I. B., Ryerson, T. B., Graus, M., Gilman, J. B., Lerner, B. M., Warneke, C., de Gouw, J. A., Middlebrook, A. M., Liao, J., Welti, A., Henderson, B. H., McNeill, V. F., Hall, S. R., Ullmann, K., Donner, L. J., Paulot, F., and Horowitz, L. W.: Observational constraints on glyoxal production from isoprene oxidation and its contribution to organic aerosol over the Southeast United States, *J. Geophys. Res.-Atmos.*, 121, 9849-9861, <https://doi.org/10.1002/2016jd025331>, 2016.

Li, K., Jacob, D. J., Liao, H., Shen, L., Zhang, Q., and Bates, K. H.: Anthropogenic drivers of 2013–2017 trends in summer surface ozone in China, *P. Natl. Acad. Sci. USA*, 116, 422–427, <https://doi.org/10.1073/pnas.1812168116>, 2019.

Li, M., Zhang, Q., Kurokawa, J. I., Woo, J. H., He, K., Lu, Z., Ohara, T., Song, Y., Streets, D. G., Carmichael, G. R., Cheng, Y., Hong, C., Huo, H., Jiang, X., Kang, S., Liu, F., Su, H., and Zheng, B.: MIX: a mosaic Asian anthropogenic emission inventory under the international collaboration framework of the MICS-Asia and HTAP, *Atmos. Chem. Phys.*, 17, 935–963, <https://doi.org/10.5194/acp-17-935-2017>, 2017.

Lin, M., Fiore, A. M., Cooper, O. R., Horowitz, L. W., Langford, A. O., Levy II, H., Johnson, B. J., Naik, V., Oltmans, S. J., and Senff, C. J.: Springtime high surface ozone events over the western United States: Quantifying the role of stratospheric intrusions, *J. Geophys. Res.-Atmos.*, 117, D00V22, <https://doi.org/10.1029/2012JD018151>, 2012a.

Lin, M., Fiore, A. M., Horowitz, L. W., Cooper, O. R., Naik, V., Holloway, J., Johnson, B. J., Middlebrook, A. M., Oltmans, S. J., Pollack, I. B., Ryerson, T. B., Warner, J. X., Wiedinmyer, C., Wilson, J., and Wyman, B.: Transport of Asian ozone pollution into surface air over the western United States in spring, *J. Geophys. Res.-Atmos.*, 117, D00V07, <https://doi.org/10.1029/2011JD016961>, 2012b.

Lin, M., Fiore, A. M., Horowitz, L. W., Langford, A. O., Oltmans, S. J., Tarasick, D., and Rieder, H. E.: Climate variability modulates western US ozone air quality in spring via deep stratospheric intrusions, *Nat. Commun.*, 6, 7105, <https://doi.org/10.1038/ncomms8105>, 2015a.

Lin, M., Horowitz, L. W., Cooper, O. R., Tarasick, D., Conley, S., Iraci, L. T., Johnson, B., Leblanc, T., Petropavlovskikh, I., and Yates, E. L.: Revisiting the evidence of increasing springtime ozone mixing ratios in the free troposphere over western North America, *Geophys. Res. Lett.*, 42, <https://doi.org/10.1002/2015GL065311>, 2015b.

Lin, M., Horowitz, L. W., Payton, R., Fiore, A. M., and Tonnesen, G.: US surface ozone trends and extremes from 1980 to 2014: quantifying the roles of rising Asian emissions, domestic controls, wildfires, and climate, *Atmos. Chem. Phys.*, 17, 2943–2970, <https://doi.org/10.5194/acp-17-2943-2017>, 2017.

Lin, M., Malyshev, S., Shevliakova, E., Paulot, F., Horowitz, L. W., Fares, S., Mikkelsen, T. N., and Zhang, L.: Sensitivity of ozone dry deposition to ecosystem-atmosphere interactions: A critical appraisal of observations and simulations, *Global Biogeochem. Cy.*, 30, <https://doi.org/10.1029/2018gb006157>, 2019.

Liu, F., Zhang, Q., van der A, R. J., Zheng, B., Tong, D., Yan, L., Zheng, Y., and He, K.: Recent reduction in NO x emissions over China: synthesis of satellite observations and emission inventories, *Environ. Res. Lett.*, 11, 114002, <https://doi.org/10.1088/1748-9326/11/11/114002>, 2016.

Mao, J., Horowitz, L. W., Naik, V., Fan, S., Liu, J., and Fiore, A. M.: Sensitivity of tropospheric oxidants to biomass burning emissions: implications for radiative forcing, *Geophys. Res. Lett.*, 40, 1241–1246, <https://doi.org/10.1002/grl.50210>, 2013a.

Mao, J., Paulot, F., Jacob, D. J., Cohen, R. C., Crounse, J. D., Wennberg, P. O., Keller, C. A., Hudman, R. C., Barkley, M. P., and Horowitz, L. W.: Ozone and organic nitrates over the eastern United States: Sensitivity to isoprene chemistry, *J. Geophys. Res.-Atmos.*, 118, 11,256–211,268, <https://doi.org/10.1002/jgrd.50817>, 2013b.

McLinden, C. A., Olsen, S. C., Hannegan, B., Wild, O., Prather, M. J., and Sundet, J.: Stratospheric ozone in 3-D models: A simple chemistry and the cross-tropopause flux, *J. Geophys. Res.-Atmos.*, 105, 14653–14665, <https://doi.org/10.1029/2000jd900124>, 2000.

Morgenstern, O., Zeng, G., Luke Abraham, N., Telford, P. J., Braesicke, P., Pyle, J. A., Hardiman, S. C., O'Connor, F. M., and Johnson, C. E.: Impacts of climate change, ozone recovery, and increasing

methane on surface ozone and the tropospheric oxidizing capacity, *J. Geophys. Res.-Atmos.*, 118, 1028-1041, <https://doi.org/10.1029/2012jd018382>, 2013.

Murray, L. T., Jacob, D. J., Logan, J. A., Hudman, R. C., and Koshak, W. J.: Optimized regional and interannual variability of lightning in a global chemical transport model constrained by LIS/OTD satellite data, *J. Geophys. Res.-Atmos.*, 117, <https://doi.org/10.1029/2012jd017934>, 2012.

Naik, V., Horowitz, L. W., Fiore, A. M., Ginoux, P., Mao, J., Aghedo, A. M., and Levy II, H.: Impact of preindustrial to present-day changes in short-lived pollutant emissions on atmospheric composition and climate forcing, *J. Geophys. Res.-Atmos.*, 118, 8086-8110, <https://doi.org/10.1002/jgrd.50608>, 2013.

Parrish, D. D., Trainer, M., Holloway, J. S., Yee, J. E., Warshawsky, M. S., Fehsenfeld, F. C., Forbes, G. L., and Moody, J. L.: Relationships between ozone and carbon monoxide at surface sites in the North Atlantic region, *J. Geophys. Res.-Atmos.*, 103, 13357-13376, <https://doi.org/10.1029/98JD00376>, 1998.

Paulot, F., Ginoux, P., Cooke, W. F., Donner, L. J., Fan, S., Lin, M. Y., Mao, J., Naik, V., and Horowitz, L. W.: Sensitivity of nitrate aerosols to ammonia emissions and to nitrate chemistry: implications for present and future nitrate optical depth, *Atmos. Chem. Phys.*, 16, 1459-1477, <https://doi.org/10.5194/acp-16-1459-2016>, 2016.

Paulot, F., Paynter, D., Ginoux, P., Naik, V., Whitburn, S., Van Damme, M., Clarisse, L., Coheur, P.-F., and Horowitz, L. W.: Gas-aerosol partitioning of ammonia in biomass burning plumes: Implications for the interpretation of spaceborne observations of ammonia and the radiative forcing of ammonium nitrate, *Geophys. Res. Lett.*, 44, 8084-8093, <https://doi.org/10.1002/2017GL074215>, 2017.

Prather, M. J., Zhu, X., Tang, Q., Hsu, J., and Neu, J. L.: An atmospheric chemist in search of the tropopause, *J. Geophys. Res.-Atmos.*, 116, <https://doi.org/10.1029/2010JD014939>, 2011.

Rasmussen, D. J. et al. Surface ozone-temperature relationships in the eastern US: a monthly climatology for evaluating chemistry-climate models. *Atmos. Environ.* 47, 142-153 (2012).

Schnell, J. L., Naik, V., Horowitz, L. W., Paulot, F., Mao, J., Ginoux, P., Zhao, M., and Ram, K.: Exploring the relationship between surface PM2.5 and meteorology in Northern India, *Atmos. Chem. Phys.*, 18, 10157-10175, <https://doi.org/10.5194/acp-18-10157-2018>, 2018.

Singh, H. B., Cai, C., Kaduwela, A., Weinheimer, A., and Wisthaler, A.: Interactions of fire emissions and urban pollution over California: Ozone formation and air quality simulations, *Atmos. Environ.*, 56, 45-51, <https://doi.org/10.1016/j.atmosenv.2012.03.046>, 2012.

Sun, L., Xue, L., Wang, T., Gao, J., Ding, A., Cooper, O. R., Lin, M., Xu, P., Wang, Z., Wang, X., Wen, L., Zhu, Y., Chen, T., Yang, L., Wang, Y., Chen, J., and Wang, W.: Significant increase of summertime ozone at Mount Tai in Central Eastern China, *Atmos. Chem. Phys.*, 16, 10637-10650, <https://doi.org/10.5194/acp-16-10637-2016>, 2016.

Travis, K. R., Jacob, D. J., Fisher, J. A., Kim, P. S., Marais, E. A., Zhu, L., Yu, K., Miller, C. C., Yantosca, R. M., Sulprizio, M. P., Thompson, A. M., Wennberg, P. O., Crounse, J. D., St. Clair, J. M., Cohen, R. C., Laughner, J. L., Dibb, J. E., Hall, S. R., Ullmann, K., Wolfe, G. M., Pollack, I. B., Peischl, J., Neuman, J. A., and Zhou, X.: Why do models overestimate surface ozone in the Southeast United States?, *Atmos. Chem. Phys.*, 16, 13561-13577, <https://doi.org/10.5194/acp-16-13561-2016>, 2016.

Trickl, T., Vogelmann, H., Fix, A., Schäfler, A., Wirth, M., Calpini, B., Levrat, G., Romanens, G., Apituley, A., Wilson, K. M., Begbie, R., Reichardt, J., Vömel, H., and Sprenger, M.: How stratospheric are deep stratospheric intrusions? LUAMI 2008, *Atmos. Chem. Phys.*, 16, 8791-8815, <https://doi.org/10.5194/acp-16-8791-2016>, 2016.

U.S. Environmental Protection Agency: Treatment of data influenced by exceptional events, edited by U. S. Environmental Protection Agency, Research Triangle Park, North Carolina, United States of America, 68216-68282 pp., 2016.

Wang, Y. X., McElroy, M. B., Jacob, D. J., and Yantosca, R. M.: A nested grid formulation for chemical transport over Asia: Applications to CO, *J. Geophys. Res.-Atmos.*, 109, <https://doi.org/10.1029/2004JD005237>, 2004.

West, J. J., Fiore, A. M., Horowitz, L. W., and Mauzerall, D. L.: Global health benefits of mitigating ozone pollution with methane emission controls, *P. Natl. Acad. Sci. USA*, 103, 3988-3993, <https://doi.org/10.1073/pnas.0600201103>, 2006.

Westerling, A. L., Hidalgo, H. G., Cayan, D. R., and Swetnam, T. W.: Warming and Earlier Spring Increase Western U.S. Forest Wildfire Activity, *Science*, 313, 940-943, <https://doi.org/10.1126/science.1128834>, 2006.

Wiedinmyer, C., Akagi, S. K., Yokelson, R. J., Emmons, L. K., Al-Saadi, J. A., Orlando, J. J., and Soja, A. J.: The Fire INventory from NCAR (FINN): a high resolution global model to estimate the emissions from open burning, *Geosci. Model Dev.*, 4, 625-641, <https://doi.org/10.5194/gmd-4-625-2011>, 2011.

Wild, R. J., Dubé, W. P., Aikin, K. C., Eilerman, S. J., Neuman, J. A., Peischl, J., Ryerson, T. B., and Brown, S. S.: On-road measurements of vehicle NO₂/NO_x emission ratios in Denver, Colorado, USA, *Atmos. Environ.*, 148, 182-189, <https://doi.org/10.1016/j.atmosenv.2016.10.039>, 2017.

Young, P. J., Naik, V., Fiore, A. M., Gaudel, A., Guo, J., Lin, M. Y., J. L. Neu, D. D. Parrish, H. E. Rieder, J. L. Schnell, S. Tilmes, O. Wild, L. Zhang, J. R. Ziemke, J. Brandt, A. Delcloo, R. M. Doherty, C. Geels, M. I. Hegglin, L. Hu, U. Im, R. Kumar, A. Luhar, L. Murray, D. Plummer, J. Rodriguez, A. Saiz-Lopez, M. G. Schultz, M. T. Woodhouse, and Zeng, G.: Tropospheric Ozone Assessment Report: Assessment of global-scale model performance for global and regional ozone distributions, variability, and trends, *Elem. Sci. Anth.*, 6(1), <https://doi.org/10.1525/elementa.265>, 2018.

Zhang, L., Jacob, D. J., Boersma, K. F., Jaffe, D. A., Olson, J. R., Bowman, K. W., Worden, J. R., Thompson, A. M., Avery, M. A., Cohen, R. C., Dibb, J. E., Flock, F. M., Fuelberg, H. E., Huey, L. G., McMillan, W. W., Singh, H. B., and Weinheimer, A. J.: Transpacific transport of ozone pollution and the effect of recent Asian emission increases on air quality in North America: an integrated analysis using satellite, aircraft, ozonesonde, and surface observations, *Atmos. Chem. Phys.*, 8, 6117-6136, <https://doi.org/10.5194/acp-8-6117-2008>, 2008.

Zhang, L., Jacob, D. J., Downey, N. V., Wood, D. A., Blewitt, D., Carouge, C. C., van Donkelaar, A., Jones, D. B. A., Murray, L. T., and Wang, Y.: Improved estimate of the policy-relevant background ozone in the United States using the GEOS-Chem global model with 1/2° × 2/3° horizontal resolution over North America, *Atmos. Environ.*, 45, 6769-6776, <https://doi.org/10.1016/j.atmosenv.2011.07.054>, 2011.

Zhang, L., Jacob, D. J., Yue, X., Downey, N. V., Wood, D. A., and Blewitt, D.: Sources contributing to background surface ozone in the US Intermountain West, *Atmos. Chem. Phys.*, 14, 5295-5309, <https://doi.org/10.5194/acp-14-5295-2014>, 2014.

Zhao, M., Golaz, J.-C., Held, I. M., Ramaswamy, V., Lin, S.-J., Ming, Y., Ginoux, P., Wyman, B., Donner, L. J., Paynter, D., and Guo, H.: Uncertainty in Model Climate Sensitivity Traced to Representations of Cumulus Precipitation Microphysics, *J. Climate*, 29, 543-560, <https://doi.org/10.1175/jcli-d-15-0191.1>, 2016.

Zhao, M., Golaz, J.-C., Held, I. M., Guo, H., Balaji, V., Benson, R., Chen, J.-H., Chen, X., Donner, L. J., Dunne, J. P., Dunne, K., Durachta, J., Fan, S.-M., Freidenreich, S. M., Garner, S. T., Ginoux, P., Harris, L. M., Horowitz, L. W., Krasting, J. P., Langenhorst, A. R., Liang, Z., Lin, P., Lin, S.-J., Malyshev, S.

L., Mason, E., Milly, P. C. D., Ming, Y., Naik, V., Paulot, F., Paynter, D., Phillipps, P., Radhakrishnan, A., Ramaswamy, V., Robinson, T., Schwarzkopf, D., Seman, C. J., Shevliakova, E., Shen, Z., Shin, H., Silvers, L. G., Wilson, J. R., Winton, M., Wittenberg, A. T., Wyman, B., and Xiang, B.: The GFDL Global Atmosphere and Land Model AM4.0/LM4.0: 2. Model Description, Sensitivity Studies, and Tuning Strategies, *Journal of Advances in Modeling Earth Systems*, 10, 735-769, <https://doi.org/10.1002/2017ms001209>, 2018a.

Zhao, M., Golaz, J.-C., Held, I. M., Guo, H., Balaji, V., Benson, R., Chen, J.-H., Chen, X., Donner, L. J., Dunne, J. P., Dunne, K., Durachta, J., Fan, S.-M., Freidenreich, S. M., Garner, S. T., Ginoux, P., Harris, L. M., Horowitz, L. W., Krasting, J. P., Langenhorst, A. R., Liang, Z., Lin, P., Lin, S.-J., Malyshev, S. L., Mason, E., Milly, P. C. D., Ming, Y., Naik, V., Paulot, F., Paynter, D., Phillipps, P., Radhakrishnan, A., Ramaswamy, V., Robinson, T., Schwarzkopf, D., Seman, C. J., Shevliakova, E., Shen, Z., Shin, H., Silvers, L. G., Wilson, J. R., Winton, M., Wittenberg, A. T., Wyman, B., and Xiang, B.: The GFDL Global Atmosphere and Land Model AM4.0/LM4.0: 1. Simulation Characteristics With Prescribed SSTs, *Journal of Advances in Modeling Earth Systems*, 10, 691-734, <https://doi.org/10.1002/2017ms001208>, 2018b.

Table 1. List of high-O₃ events above 65 ppbv in the greater Las Vegas region during April-June 2017 (unit: ppbv).

Events	MDA8 O ₃ (1-min max) at Angel Peak	Simulated MDA8 O ₃ (USB) at Angel Peak: AM4 vs. GC	MDA8 O ₃ at Clark County sites	Maximum MDA8 O ₃ at rural sites in affected regions	Observed ΔO ₃ /ΔCO	Observed d H ₂ O (g/kg)	Vertical profiles; synoptic maps	Surface impacts
Stratospheric intrusions								
April 22-23	-	66 vs. 53 (60 vs. 47)	SM Youth Camp: 70; Green Valley: 67	Apr 22: WY: Centennial (76); CO: Mesa Verde NP (72), Gothic (82) Apr 23: WY: Centennial (75); CO: Rocky Mt. NP (70); CA: Joshua Tree (76)	-	-	Fig. S5	Figs. 4 and S5
May 13-14	-	66 vs. 52 (62 vs. 48)	May 13: SM Youth Camp: 70; May 14: SM Youth Camp: 71	May 13: CA: Joshua Tree (74); UT: AQs site: Zion NP (69) May 14: NV: Great Basin NP (65)	-	-	Fig. S5	Figs. 4 and S5
June 11-13	June 11: 66 (84)	65 vs. 47 (58 vs. 42)	Jun 11: SM Youth Camp: 64	Jun 12: WY: Centennial (70); CO: Mesa Verde (69) Jun 13: WY: Centennial (65); AZ: Petrified Forest (65); AQs sites: Payson (76); NM: AQs sites: Cayote (71)	-3.79	0.6±0.2	Figs. 7-8a	Fig. 9
Combined stratospheric and regional pollution influences								
June 14	73 (80)	69 vs. 57 (53 vs. 50)	Joe Neal: 74 North LV Airport: 73, Walter Johnson: 71	CA: Joshua Tree (95); AZ: Petrified Forest (71); NM: site: Bernalillo (71)	0.75	2.5±0.3	Fig. 8b	Fig. 9
Wildfires								
June 22	67 (83)	58 vs. 76 (44 vs. 62)	Joe Neal: 78 North LV Airport: 82	CA: Sequoia NP (86); Joshua Tree (74)	0.015	3.5±0.2	Fig. 10a and 11a	Fig. 12a
Regional/local pollution events								
June 2	71 (78)	61 vs. 64 (51 vs. 49)	Joe Neal: 66 Walter Johnson: 69	CA: Joshua Tree (68, Jun 1: 79)	1.09	2.8±0.3	Fig. S10	Fig. S11
June 16	72 (82)	65 vs. 63 (46 vs. 54)	Joe Neal: 75 Palo Verde: 75 Jun 29: Joe Neal: 70; North LV Airport: 74	CA: Joshua Tree (98); AZ: Petrified Forest (65), AQs site: Payson (76)	0.68-0.70	2.6±0.4	Fig. 11b	Fig. 12b
June 29-30	June 29: 71 (78) June 30: 75 (86)	55 vs. 62 (41 vs. 54)	Jun 30: Joe Neal: 75; Walter Johnson: 75	Jun 29: CA: Sequoia NP (74); Joshua Tree (75) Jun 30: CA: Sequoia NP (83); Joshua Tree (96); AZ: Grand Canyon (66)	0.69-1.07	2.8±0.3	Fig. S10	Fig. S11
Long-range transport of Asian pollution; possibly mixed with local pollution								
May 24	65 (74)	62 vs. 68 (48 vs. 54)	Arden Peak: 72, SM Youth Camp: 66, Jean: 66, Palo Verde: 65	CA: Yosemite NP (70); ID: AQs site: Butte (69); WY: Yellowstone NP (64); UT: AQs site: Zion NP (65)	-	-	Figs. 13-14a	Fig. 15a
Unattributed event								
June 28	68 (84)	53 vs. 59 (43 vs. 54)	Joe Neal: 75; North LV Airport: 74	CA: Sequoia NP (70); AZ: Grand Canyon (66)	1.92	1.7±0.1	Fig. 10b	Fig. 15b

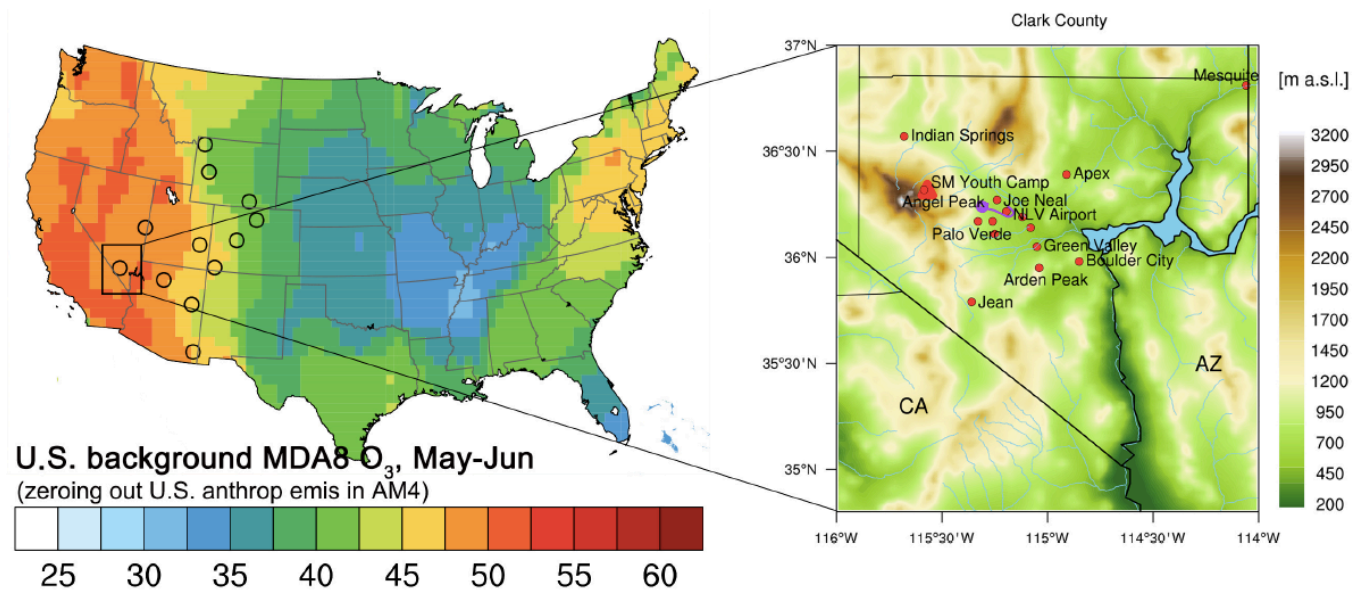


Figure 1. (Left) Mean U.S. background MDA8 O_3 (ppbv) during *FAST-LVOS* (May–June, 2017) estimated by zeroing out U.S. anthropogenic emissions in the global high-resolution (~ 50 km \times 50 km) version of the GFDL-AM4 model (circles denote 12 selected high-elevation CASTNet sites); (Right) Topographic map of Clark County displaying the locations of Angel Peak (filled triangle) and regulatory O_3 monitoring sites (filled circles). The purple trace denotes the Scientific Aviation flight track during 19:15-19:35 UTC of June 28, 2017. The topographic data is from NOAA’s National Centers for Environmental Information (<http://www.ngdc.noaa.gov/mgg/global>).

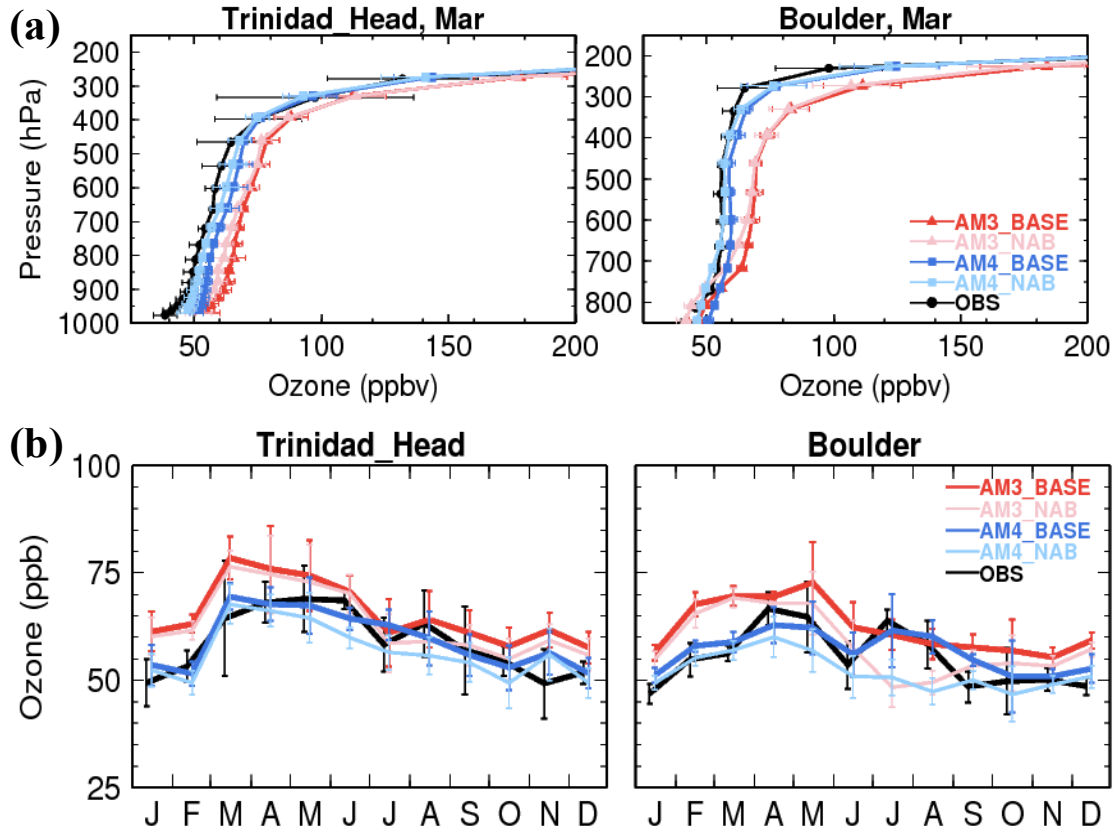


Figure 2. (a) Vertical profiles of O_3 in March and (b) monthly mean O_3 in the middle troposphere (500–430 hPa) at Trinidad Head, California (41.1°N , 124.2°W , 107 m a.s.l.) and Boulder, Colorado (40.0°N , 105.0°W , 1584 m a.s.l.) during 2010–2014 as observed (black) and simulated by GFDL-AM3 (red; AM3_BASE; Lin et al., 2017) and GFDL-AM4 (blue; AM4_BASE), together with simulated North American Background O_3 (NAB; estimated with North American anthropogenic emissions zeroed out). The bars represent the standard deviations of monthly values during 2010–2014.

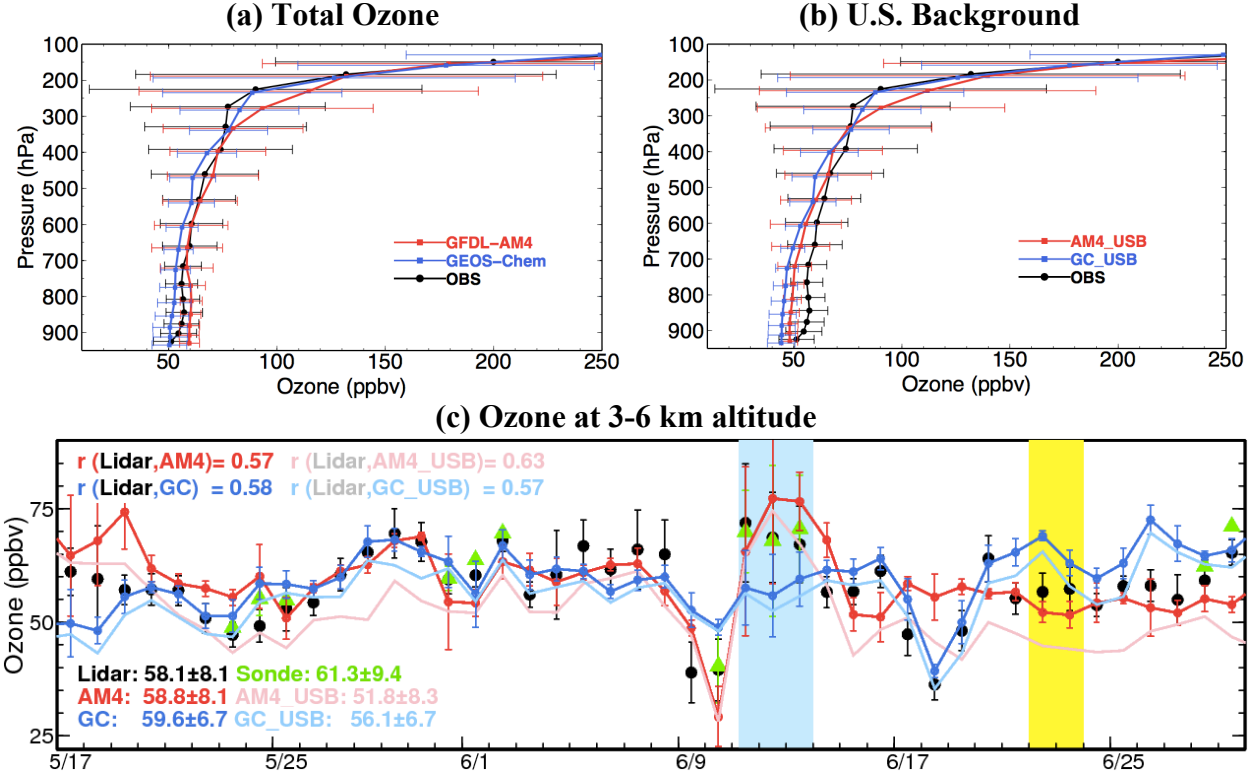


Figure 3. (a) Mean vertical O₃ profiles at Joe Neal as observed with ozonesondes (black; 30 launches) and simulated with GFDL-AM4 (red) and GEOS-Chem (blue) during *FAST-LVOS* (May–June 2017). Horizontal bars represent the standard deviations across daily profiles; (b) Same as (a), but showing U.S. background (USB) O₃ estimated by the two models. (c) Time series of O₃ averaged over 3–6 km altitude above NLVA during *FAST-LVOS* as observed (black: lidar; green: ozonesonde) and simulated with GFDL-AM4 (thick red line) and GEOS-Chem (thick dark blue line), together with simulated USB O₃ (light lines). Here and in other figures, AM4_USB represents USB estimated by GFDL-AM4 and GC_USB represents USB estimated by GEOS-Chem. The blue shading highlights the period with stratospheric intrusions and the yellow shading, the wildfire event. Vertical bars represent the standard deviations across hourly averages.

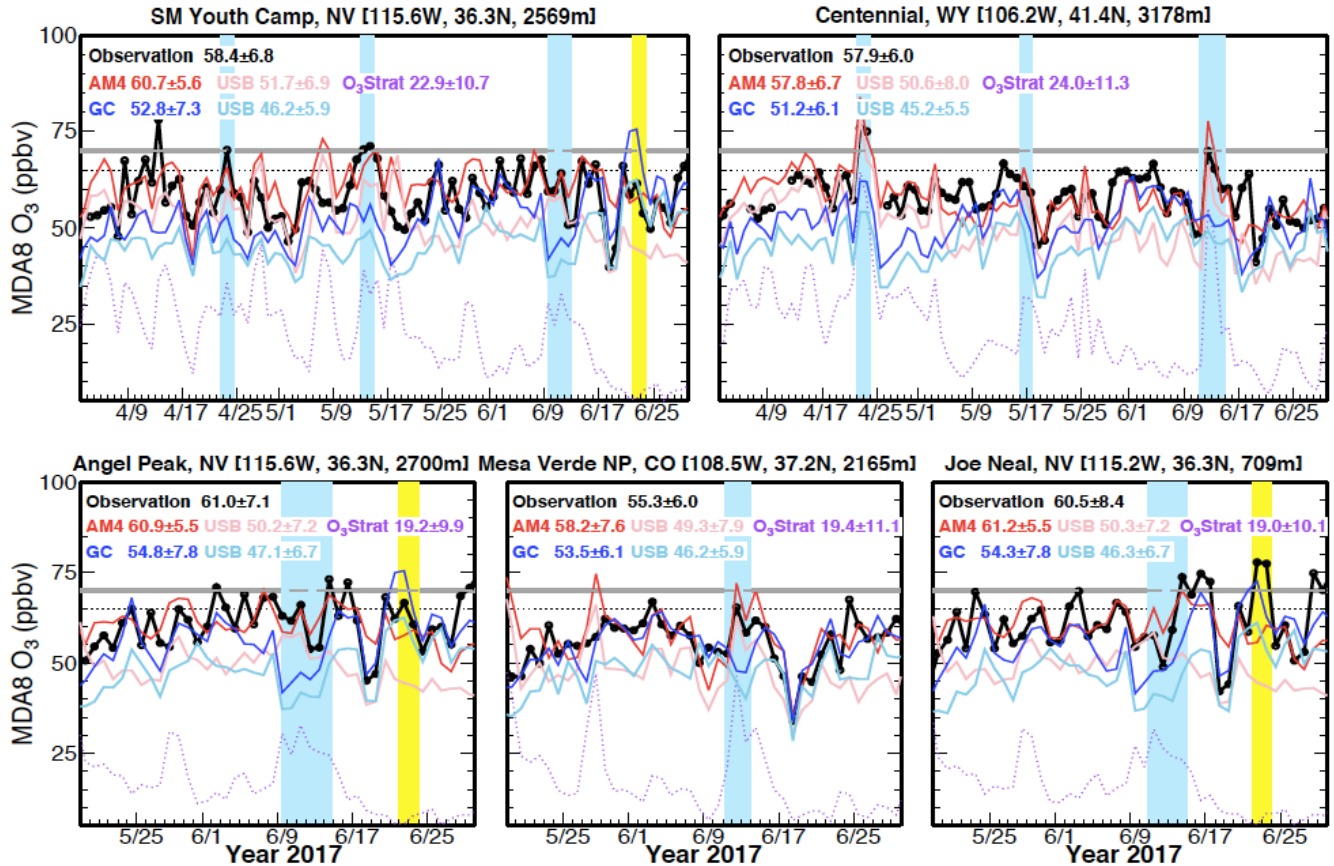


Figure 4. Time series of daily MDA8 O₃ at Spring Mountain Youth Camp (SMYC) in Nevada and Centennial in Wyoming from April to June, and at Angel Peak, Mesa Verde, and Joe Neal during the *FAST-LVOS* study period, highlighting stratospheric intrusion events (blue shading) and wildfire events (yellow shading). The SMYC O₃ monitor is located only about 125 m below, and 800 m west of the Angel Peak summit where the mobile lab was parked. Shown are total MDA8 O₃ from observations (black) and simulations by GFDL-AM4 (red) and GEOS-Chem (blue), together with USB O₃ from GFDL-AM4 (pink) and GEOS-Chem (light blue). The dashed purple line shows AM4 stratospheric O₃ tracers. The horizontal lines denote the current NAAQS level of 70 ppbv and a possible future standard of 65 ppbv.

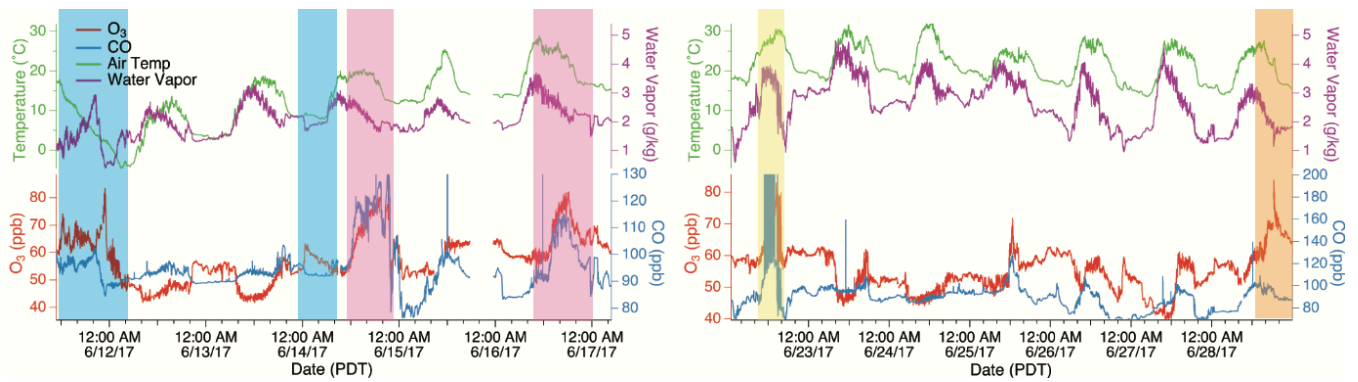


Figure 5. Time series of 1-minute averaged air temperature, water vapor, O_3 , and CO mixing ratios measured by the NOAA mobile lab deployed at Angel Peak during June 11–16 and June 22–28, 2017, highlighting the periods with stratospheric influence (blue), regional anthropogenic pollution plumes (pink), wildfire plumes (yellow), and the unattributed pollution plume (orange). Data are shown in Pacific Daylight Time (PDT). Note that peak CO mixing ratios on June 22 were 440 ppbv (not shown on the plot).

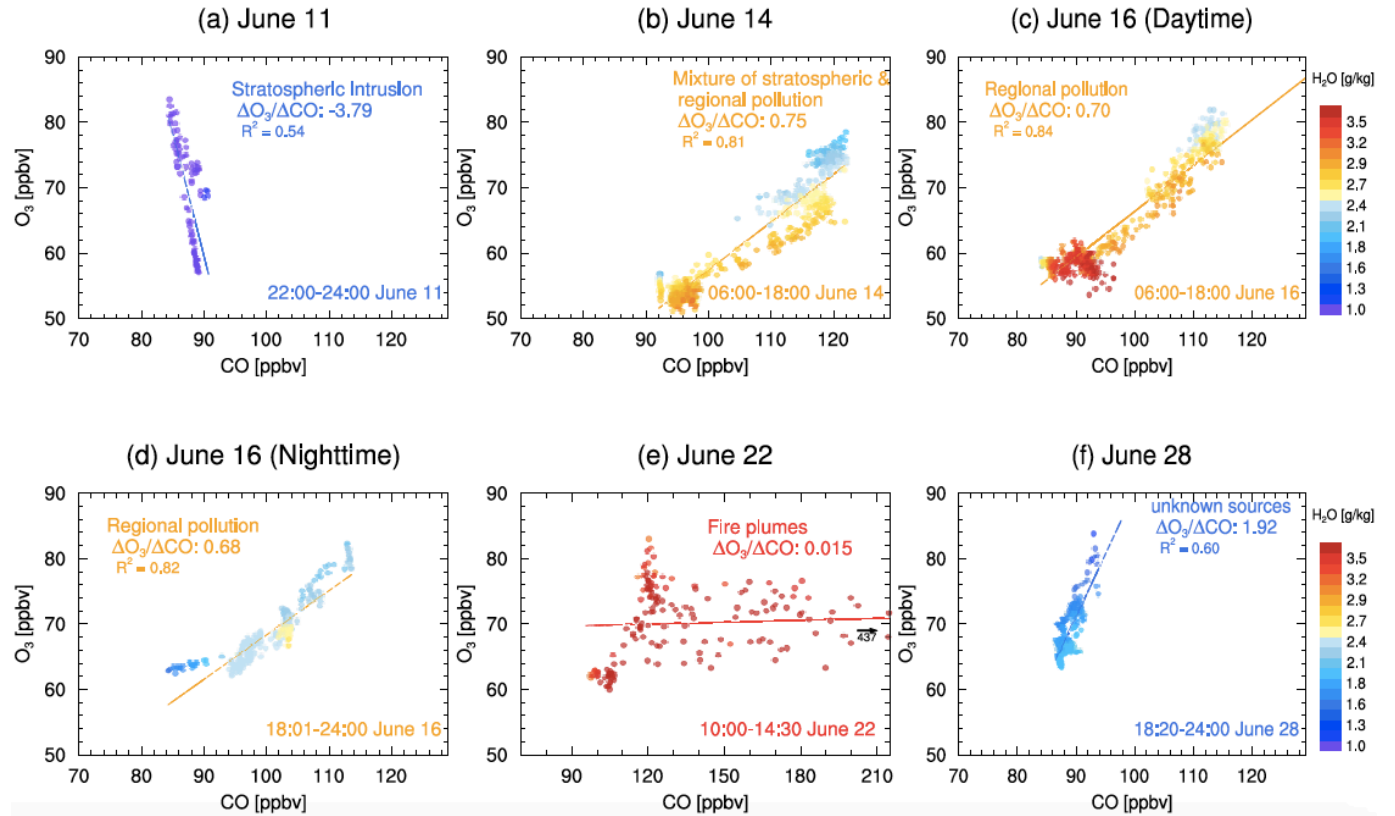


Figure 6. Scatter plots of 1-min average O₃ against CO measured at Angel Peak, color-coded by specific humidity, for air masses influenced by (a) STT on June 11; (b) regional pollution on June 14; (c–d) regional pollution plume during daytime (06:00–18:00) and nighttime (18:01–24:00) on June 16; (e) wildfires on June 22; and (f) unattributed pollution on June 28. Note that peak CO mixing ratios on June 22 were 440 ppbv (not shown on the plot).

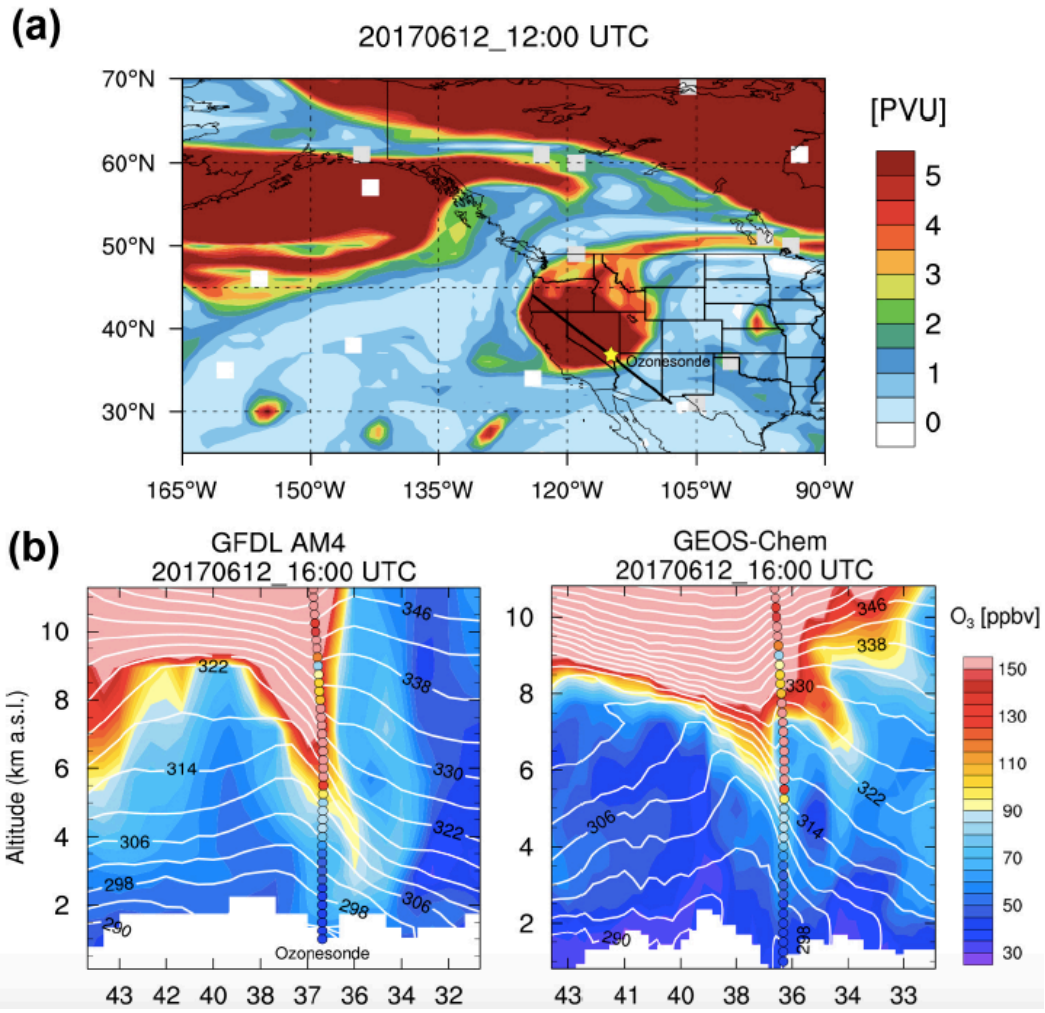


Figure 7. (a) Potential vorticity at 250 hPa on June 12 calculated from the NCEP-FNL reanalysis (PVU: $10^{-6} \text{ m}^2 \text{ s}^{-1} \text{ K kg}^{-1}$); (b) vertical distributions of O₃ (color shading) and isentropic surfaces (white lines) along a transect crossing Nevada (black line on PV map) simulated with GFDL-AM4 (left) and GEOS-Chem (right) on June 12. The color-coded circles denote ozonesonde observations at Joe Neal (star on the PV map).

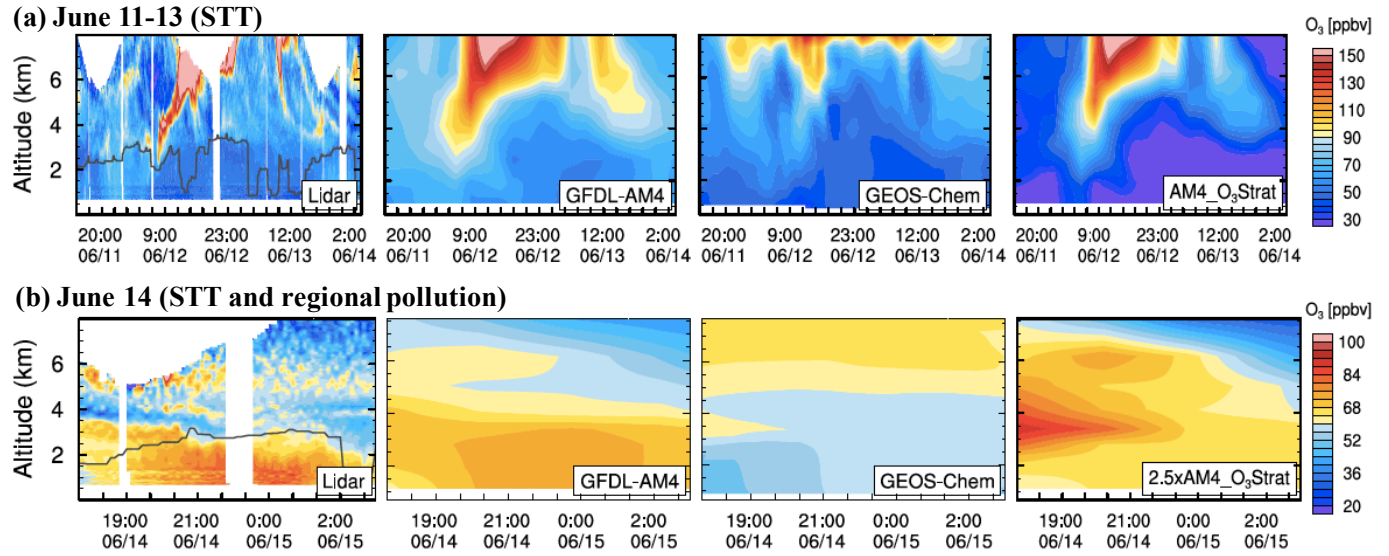
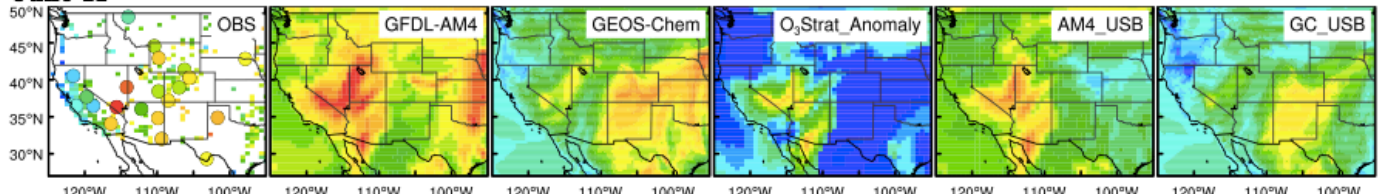
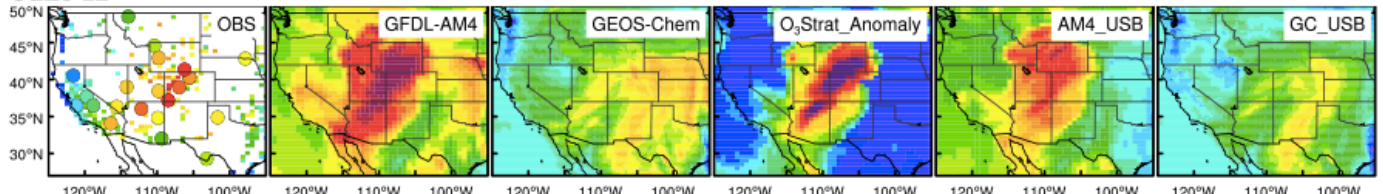


Figure 8. Time-height curtain plots of O_3 above NLVA as observed with TOPAZ lidar and simulated with GFDL-AM4 (~ 50 km \times 50 km; interpolated from 3-hourly data) and GEOS-Chem ($0.25^\circ \times 0.3125^\circ$; interpolated from hourly data) during the STT event on (a) June 11–13 and (b) June 14, 2017 (UTC). The rightmost panel shows AM4 stratospheric O_3 tracer (AM4_O3Strat). Note that AM4_O3Strat for June 14 is scaled by a factor of 2.5 for clarity. Here and in other figures, the solid black lines in the O_3 lidar plots represent boundary layer height inferred from the micro-Doppler lidar measurements.

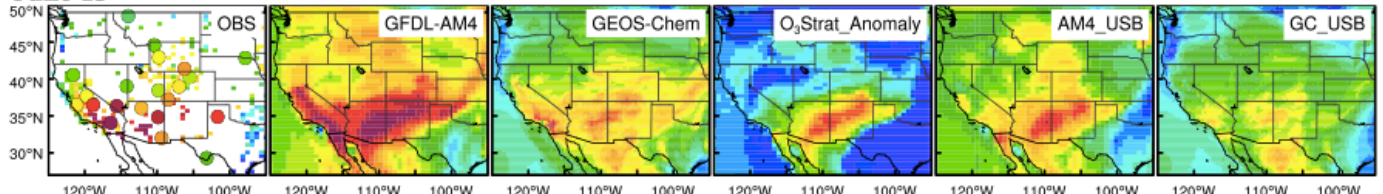
June 11



June 12



June 13



June 14

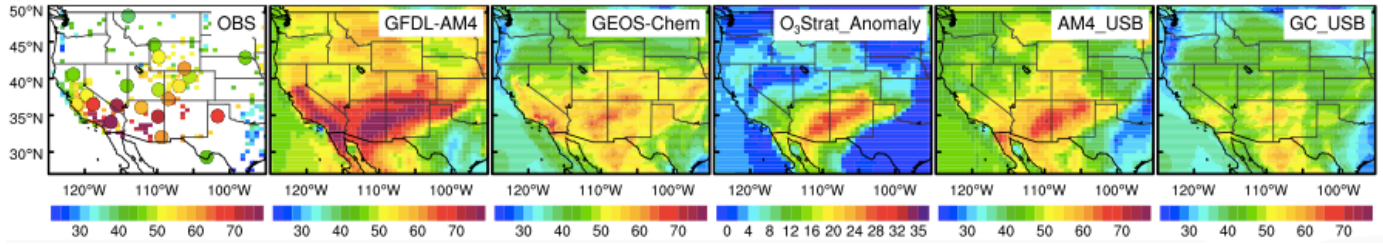


Figure 9. Maps of total MDA8 O₃ (ppbv) in surface air as observed and simulated with GFDL-AM4 and GEOS-Chem, along with anomalies in AM4 O₃Strat (relative to June mean) and model-estimated USB levels, during the STT event on June 11–14, 2017.

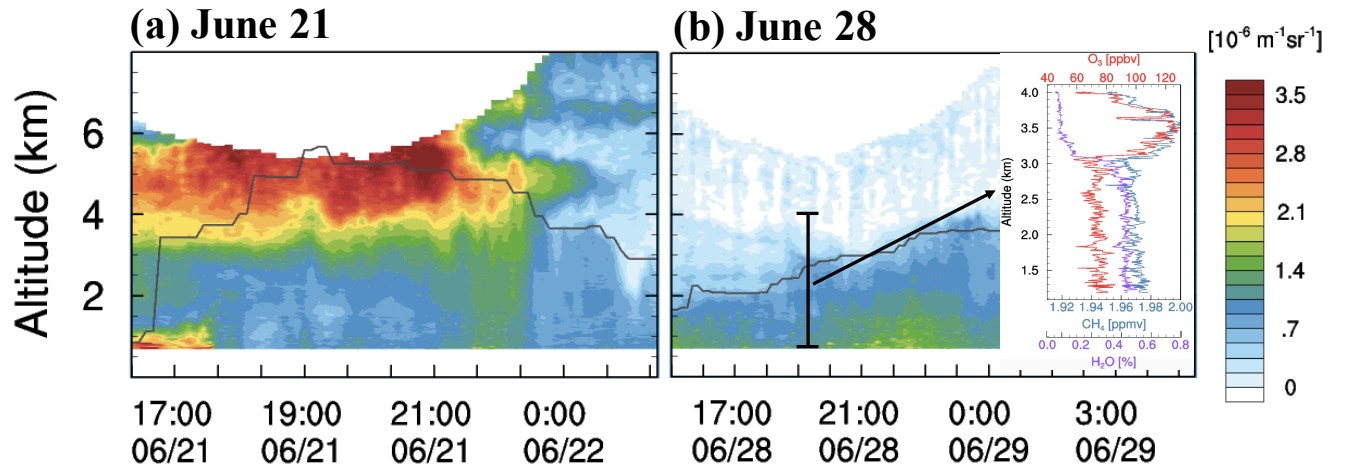


Figure 10. Time-height curtain plots of the TOPAZ aerosol backscatter above the North Las Vegas Airport during June 21–22 (a) and June 28, 2017 (b). Data are shown at UTC time. The inset graph in (b) shows vertical profiles of water vapor (purple), CH_4 (blue), and O_3 (red) measured by the Scientific Aviation flight above the Las Vegas Valley during 19:15–19:35 June 28 (UTC) (flight track in Figure 1).

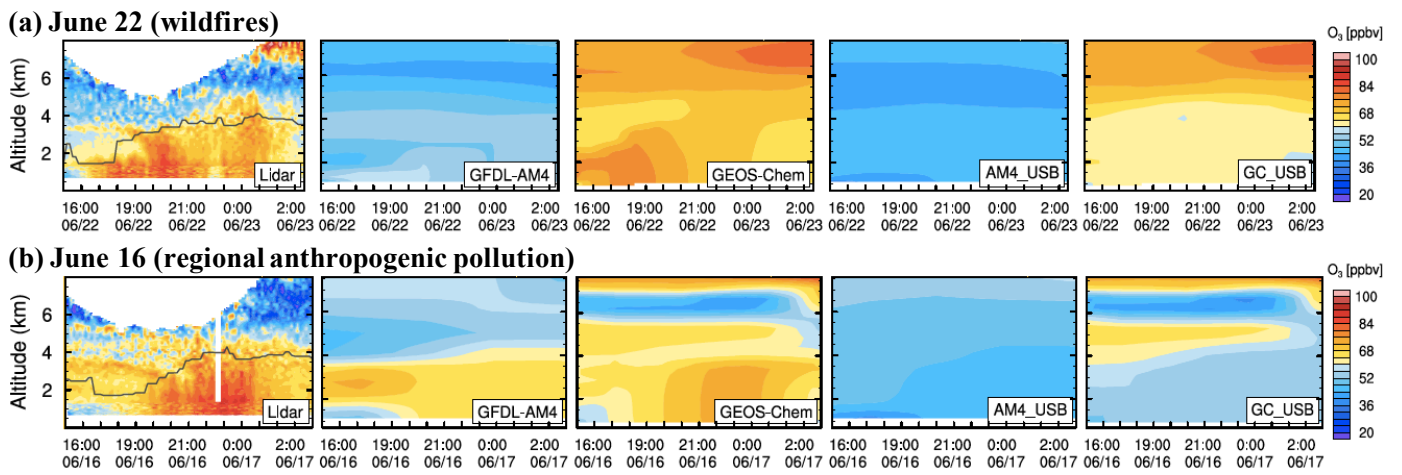
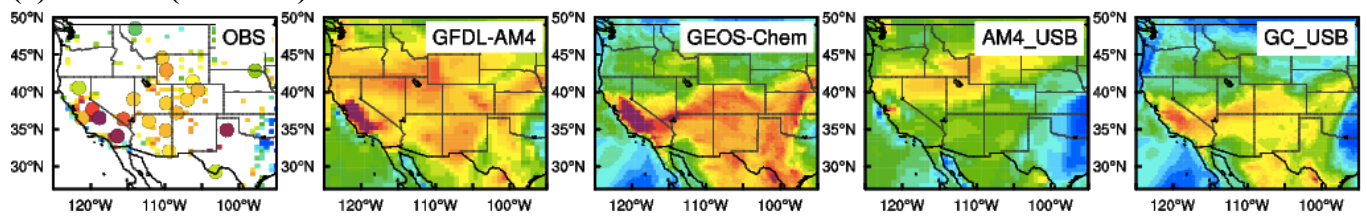


Figure 11. Same as Figure 8, but for (a) the wildfire event on June 22 and (b) the regional anthropogenic pollution event on June 16, 2017 (UTC). The right panels compare USB O₃ from the two models.

(a) June 22 (wildfires)



(b) June 16 (regional anthropogenic pollution)

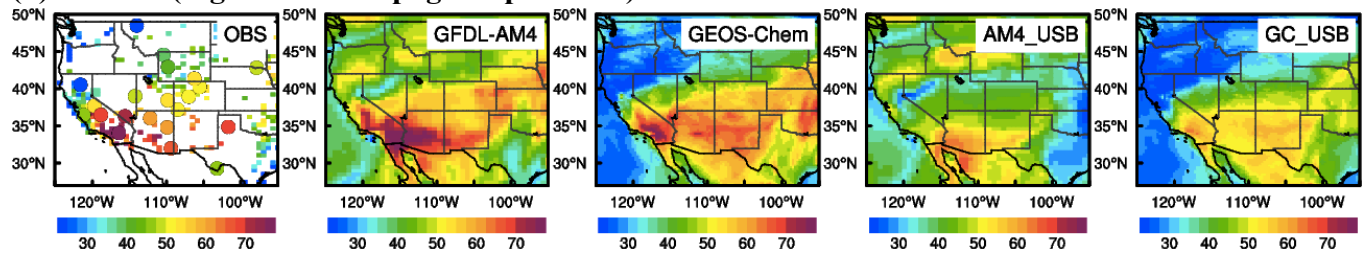


Figure 12. Same as Figure 9, but for (a) the wildfire event on June 22 and (b) the regional anthropogenic pollution event on June 16, 2017.

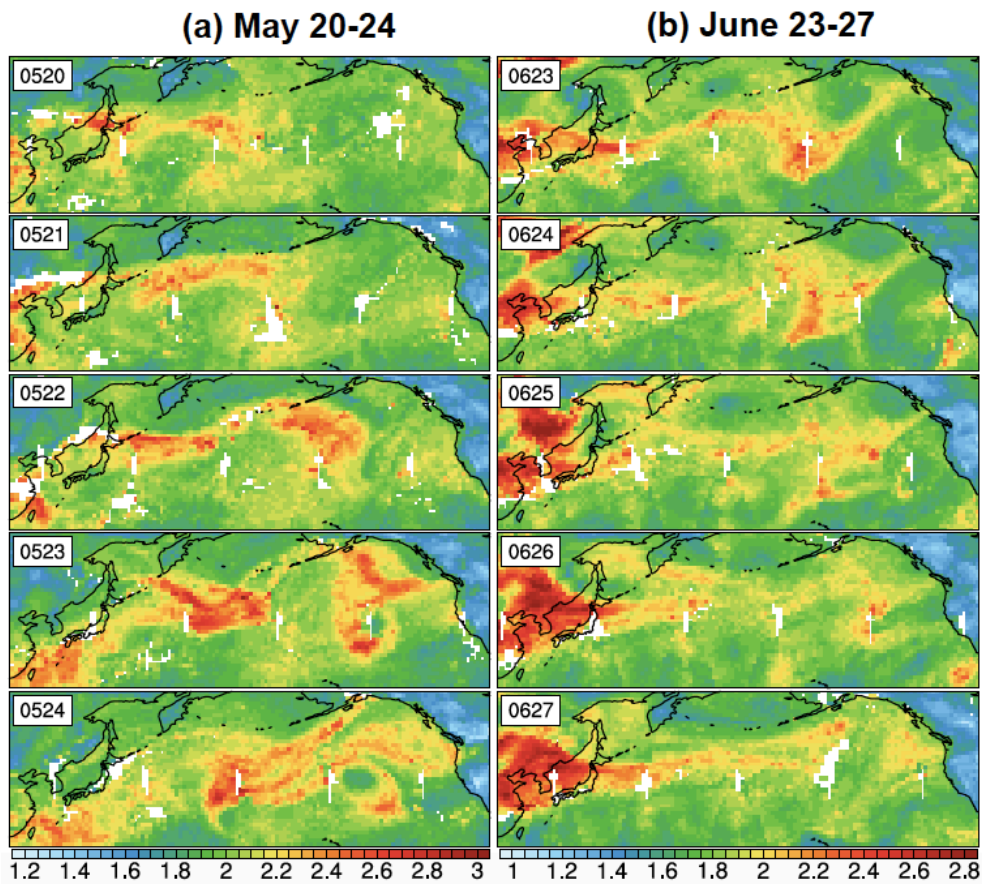
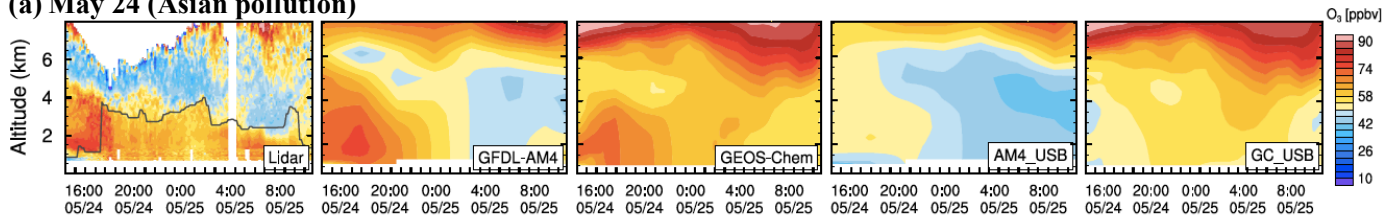


Figure 13. Trans-Pacific transport of Asian pollution plumes during (a) May 20–24 and (b) June 23–27, 2017, as seen in the NASA AIRS retrievals of CO total column (10^{18} molecules/cm 2 ; level 3 daily $1^\circ \times 1^\circ$ gridded products).

(a) May 24 (Asian pollution)



(b) June 28 (unattributed event)

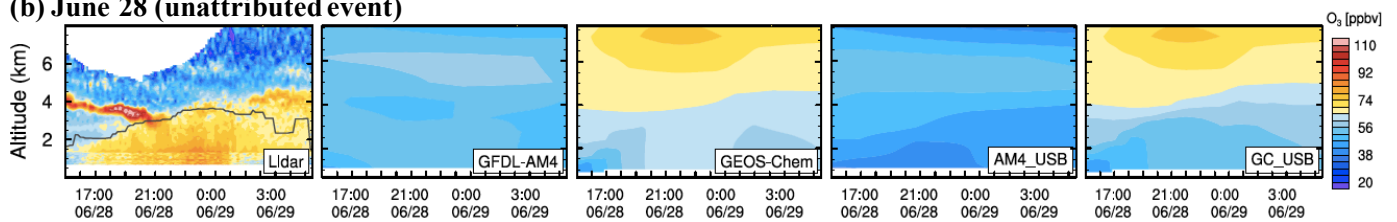
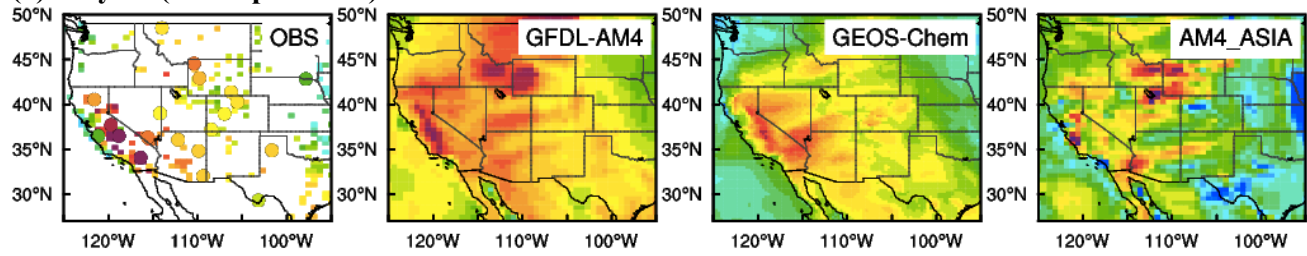


Figure 14. Same as Figure 8, but for (a) the Asian pollution event on May 24 and (b) the unattributed pollution event on June 28, 2017 (UTC).

(a) May 24 (Asian pollution)



(b) June 28 (unattributed event)

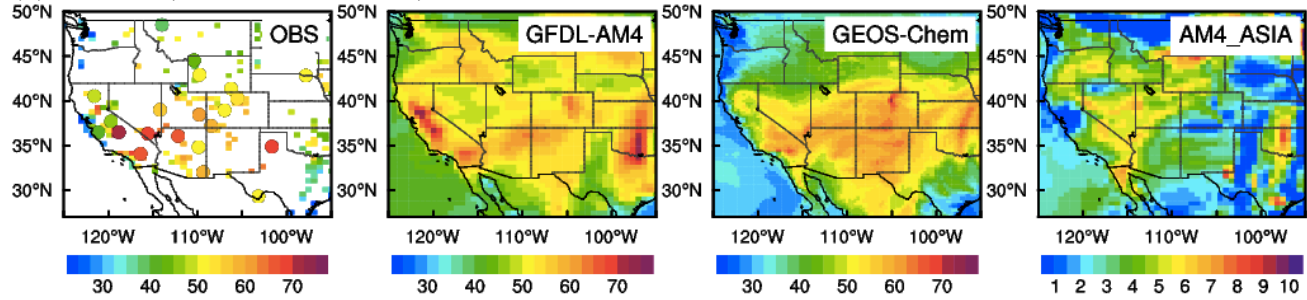


Figure 15. Same as Figure 9, but for (a) the Asian pollution event on May 24 and (b) the unattributed pollution event on June 28, 2017. The right panels show O₃ enhancements from Asian pollution estimated by GFDL-AM4.

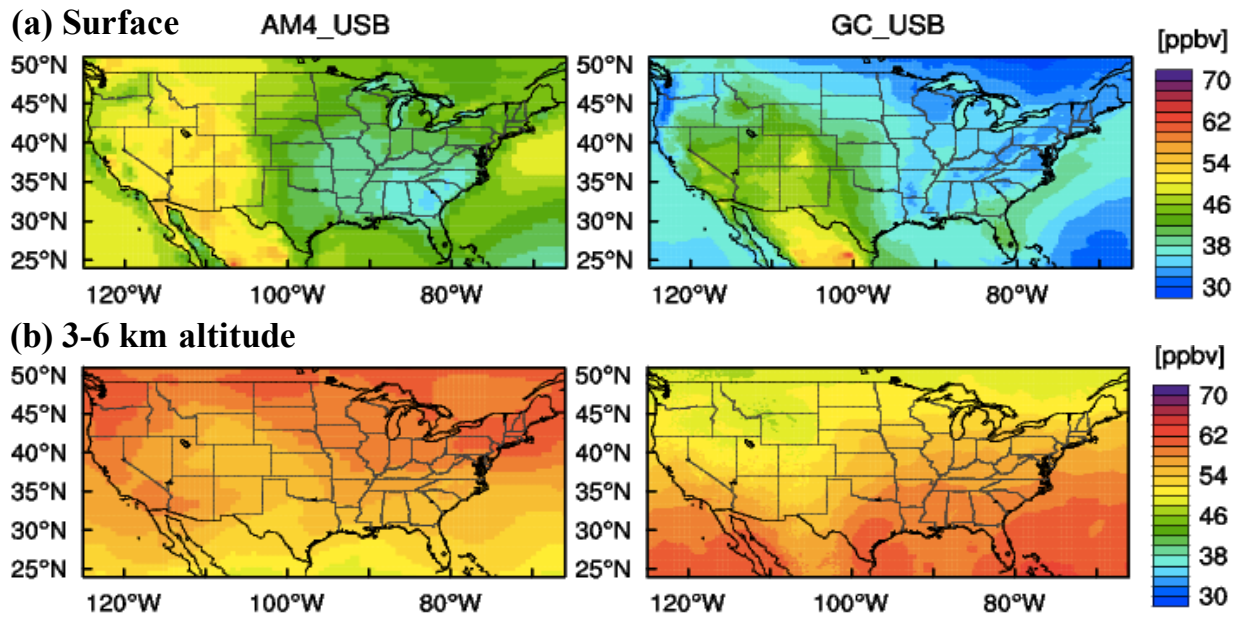


Figure 16. Spatial distributions of USB O₃ simulated with GFDL-AM4 and GEOS-Chem (a) at the surface (MDA8) and (b) at 3–6 km altitude (24-hour mean) during April–June, 2017.

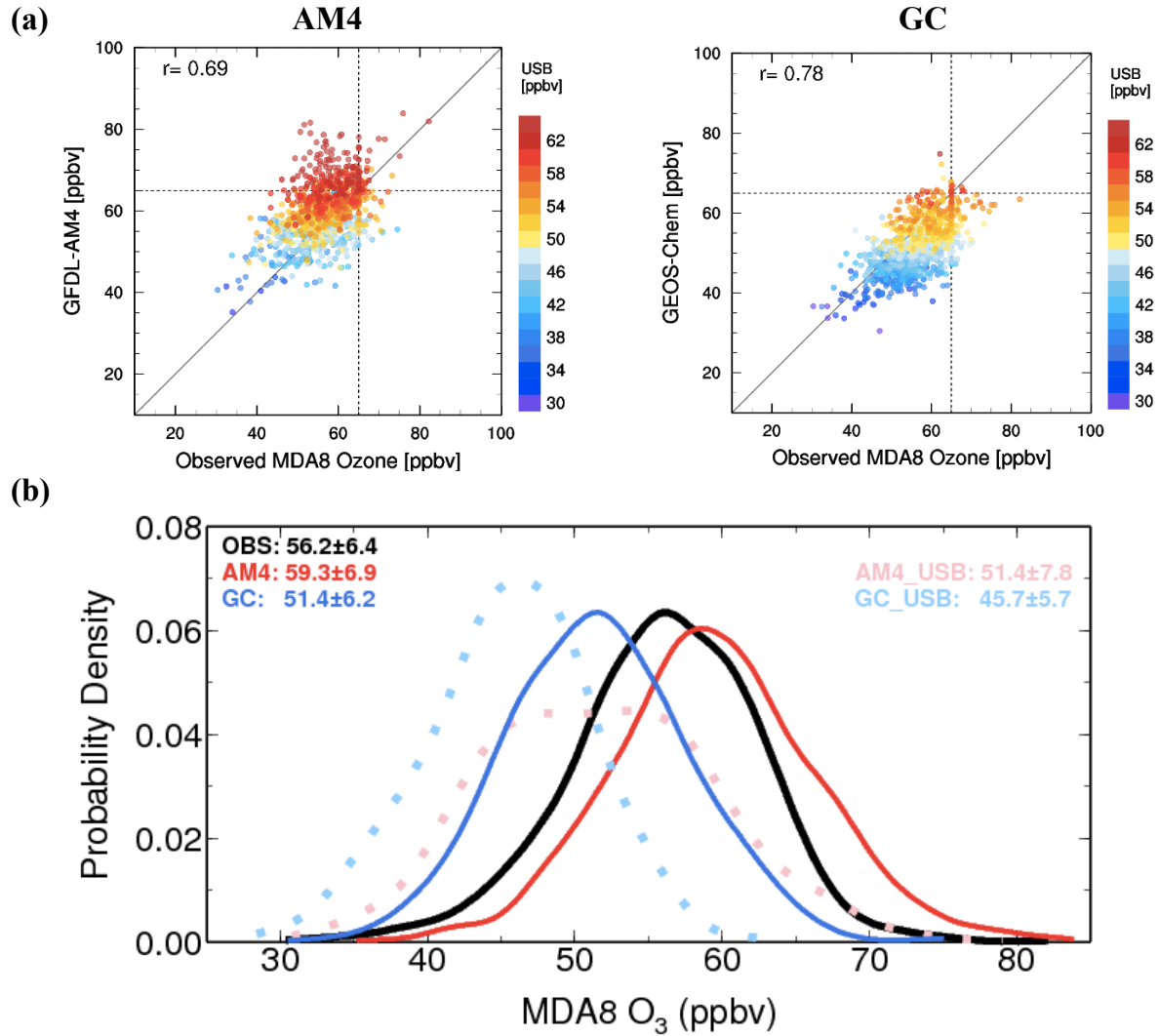


Figure 17. (a) Scatter plots of observed versus simulated daily MDA8 O₃, color-coded by USB O₃, at 12 WUS high-elevation sites (circles in Figure 1a) during April–June, 2017. The dashed lines mark the 65-ppbv threshold; (b) Probability density of daily MDA8 O₃ as observed (solid black) and simulated with GFDL-AM4 (solid red) and GEOS-Chem (solid blue), along with the distribution of USB O₃ estimated from each model (dotted lines).